Chemical Engineering Journal 530 (2026) 173306

Contents lists available at ScienceDirect

Chemical Engineering Journal

journal homepage: www.elsevier.com/locate/cej

One-step facile synthesis of polyphenol-assisted gold-platinum core-shell nanozymes for multi-enzyme mimicry in diabetic wound repair

Hafez Jafari [a,b], Lizhao Yan [c], Elham Dehghanpisheh [d], Pejman Ghaffari-bohlouli [b], Erika Hendrickx [e], Louise Conrard [e], Gian-Marco Rignanese [d], Lei Nie [f], Armin Shavandi [b,*], Peter Dubruel [a,*]

[a] Polymer Chemistry & Biomaterials Group, Centre of Macromolecular Chemistry, Department of Organic and Macromolecular Chemistry, Ghent University, Krijgslaan 281, Building S4, 9000, Ghent, Belgium
[b] 3BIO-BioMatter, École Polytechnique de Bruxelles, Université Libre de Bruxelles, Avenue F.D. Roosevelt, 50-CP 165/61, Brussels, 1050, Belgium
[c] Department of Plastic Surgery, Zhongnan Hospital of Wuhan University, Wuhan, 430071, China
[d] UCLouvain, Institute of Condensed Matter and Nanosciences (IMCN), Chemin des Étoiles 8, Louvain-la-Neuve, 1348, Belgium
[e] Center for Microscopy and Molecular Imaging (CMMI), Université Libre de Bruxelles, Rue Adrienne Bolland 10, 6041, Gosselies, Belgium
[f] College of Life Sciences, Xinyang Normal University, Xinyang, 464000, China

ARTICLE INFO

Keywords:
Diabetic foot ulcer therapy
Multi-enzyme-mimicking nanozymes
Hypoxia
Hyperglycemia

ABSTRACT

Diabetic wounds are a significant clinical challenge due to chronic inflammation, persistent oxidative stress, hyperglycaemic and hypoxic conditions, bacterial infections, and impaired tissue regeneration, all of which delay healing and increase complications. Addressing these multifaceted issues requires innovative therapeutic strategies capable of modulating the diabetic wound microenvironment. Herein, we developed a polyphenol-assisted gold-platinum (AuPt) core-shell nanozyme with multi-enzyme mimetic activities, including glucose oxidase (GOD), catalase (CAT), superoxide dismutase (SOD), peroxidase (POD), and oxidase (OXD)-like functions. Computational insights based on density functional theory (DFT) further supported the Au–Pt synergistic design. By synergistically combining the catalytic properties of Au and Pt, the nanozyme modulate oxidative stress, and reduces inflammation while promoting fibroblast viability and context-dependent antibacterial activity under acidic, ROS-rich conditions relevant to inflamed wound sites. In vivo experiments using a diabetic mouse model revealed that the developed AuPt nanozymes promoted wound healing by improving epidermal regeneration and collagen synthesis while suppressing pro-inflammatory cytokines, including TNF-α and IL-1β. These results highlight the potential of polyphenol-assisted AuPt nanozymes as a robust and multifunctional therapy to address key pathological barriers in diabetic wound healing, providing a foundation for future clinical applications.

1. Introduction

Impaired wound healing in diabetic patients, such as diabetic foot ulcers (DFUs), a common consequence of persistent hyperglycemia, poses a substantial burden due to its high rates of morbidity and mortality. It frequently leads to recurrent infections and is a major cause of non-traumatic limb amputations globally [1]. Beyond diabetes, a variety of chronic diseases contribute to chronic wounds, including cardiovascular disease, cerebrovascular disease, immunosuppression, infection, and repetitive trauma [2]. A high glucose environment in diabetic wounds may hinder the normal wound healing process due to the impairments in keratinocyte physiology and function, as well as decreasing blood circulation and oxygen delivery to the wound site [3]. Additionally, the diabetic wound environment is marked by uncontrolled accumulation of reactive oxygen species (ROS) and chronic hypoxia, which disrupt the balance between proinflammatory and anti-inflammatory macrophages, thereby inhibiting the viability of endogenous stem cells, the synthesis of extracellular matrix (ECM), and growth factor function [4,5].

Although significant strides have been made in diabetic wound care, current therapeutic options, such as wound dressing hydrogels, offering benefits such as high porosity, soft consistency, adjustable mechanical properties, and support for cell proliferation, still fall short in addressing the complex needs of diabetic wound healing [6–8]. These materials,

* Corresponding authors.
E-mail addresses: nielei@xynu.edu.cn (L. Nie), armin.shavandi@ulb.be (A. Shavandi), Peter.Dubruel@UGent.be (P. Dubruel).

https://doi.org/10.1016/j.cej.2026.173306
Received 30 September 2025; Received in revised form 18 December 2025; Accepted 21 January 2026
Available online 22 January 2026

although advanced, typically do not provide active therapeutic functions that directly counteract the underlying pathophysiological processes, such as oxidative stress, hyperglycemia, hypoxia, and impaired angiogenesis, prevalent in DFUs.

To effectively advance healing outcomes in DFUs, there is a compelling demand for a transition from passive to more innovative materials that can participate in the healing process. In this regard, nanozymes, with their intrinsic multi-enzyme-mimicking capabilities, can dynamically interact with the biological environment [9,10]. Compared to natural enzymes, nanozymes are favorable for participating in complex biocatalytic processes in wound healing due to their high stability, lower sensitivity to external conditions, and ease of production and storage [11]. Among different classifications of nanozymes such as carbon-derived nanozymes [12,13], noble metal nanozymes [14], metal oxide nanozymes [15,16], and metal-organic framework (MOFs) [17,18], noble metal nanozymes are gaining significant attention due to their copious electric charges, excellent stability, adjustable catalytic capacity, and accessibility for surface alteration [19].

Among the noble metals, gold nanozyme (Au) exhibits glucose oxidase (GOD)-mimicking activity, catalyzing the oxidation of glucose to generate hydrogen peroxide (H_2O_2), similar to natural enzymes. This property may contribute to mitigating hyperglycemic conditions in diabetic wounds [20]. However, oxygen consumption and ROS generation during the GOD reaction can intensify hypoxic conditions and oxidative stress, which adversely affect the healing process [21]. Hence, there is a need to compensate for the oxygen consumption and ROS generation during the GOD reaction. In this regard, platinum nanozyme (Pt) has shown high peroxidase-like activity (POD) [22], catalase-like activity (CAT) [23], and superoxide dismutase-like activity (SOD) [24]. Compared with transition-metal nanozymes such as Fe-, Mn-, or Se-based systems, which mainly exhibit single peroxidase or catalase activity, Au and Pt were selected for their complementary catalytic functions. Au uniquely displays glucose oxidase (GOD)-like activity, while Pt provides superior catalytic efficiency toward H_2O_2 decomposition and radical regulation.

Therefore, a synergistic combination of gold and platinum nanozymes presents a promising strategy to maintain natural redox balance during wound healing process. The glucose oxidase-like (GOD) activity of gold nanozyme catalyzes glucose oxidation and generates H_2O_2. This H_2O_2 serves a dual role; it acts as a substrate for the peroxidase-like (POD) activity of Pt, which breaks it down into hydroxyl radicals (OH•), and other ROS in smaller quantities to combat bacterial infection [25]. The H_2O_2 is also converted into oxygen through the catalase-like (CAT) activity of platinum nanozyme. While the exact balance between oxygen consumption during glucose oxidation and oxygen production via catalase activity has yet to be fully quantified, the process is expected to help alleviate oxidative stress by producing oxygen. The proposed oxygen-modulating effect is expected to be local and context-dependent rather than a global correction of tissue oxygenation. Additionally, the superoxide dismutase-like (SOD) activity of platinum nanozymes reduces superoxide radicals into hydrogen peroxide (H_2O_2), with their CAT activity further transforming any residual H_2O_2 into oxygen, enhancing the wound environment for improved healing. Hence, Au nanozymes first catalyze the oxidation of glucose in a hyperglycemic environment, producing H_2O_2 at physiological pH (~pH 7), particularly relevant in diabetic wounds, where elevated glucose levels induce oxidative stress. The residual H_2O_2 generation may still provide substrate for Pt-mediated POD activity under acidic conditions, contributing to localized antibacterial effects.

In parallel, the superoxide dismutase (SOD)-like activity of Pt converts superoxide radicals into H_2O_2 at neutral pH, alongside their catalase-like (CAT) activity, which transforms H_2O_2 into oxygen. The ultimate aim of this system is to manage oxidative stress caused by hyperglycemia, while simultaneously producing controlled ROS for antibacterial effects and generating oxygen to relieve hypoxia, thereby promoting wound healing.

In this regard, a few studies have investigated AuPt nanozymes for wound healing. Zhang et al. synthesized AuPt alloys via $NaBH_4$ reduction for diabetic wound dressings [26]. Wu et al. synthesized core–shell Au@Pt nanoparticles using a PVP-assisted seed-mediated method via microwave synthesis and demonstrated peroxidase-like activity [27]. Zhang et al. employed a peptide-templated biomineralization approach using capreomycin to produce bimetallic AuPt nanoparticles with oxidase- and peroxidase-like properties [28]. However, these systems often rely on multistep synthesis, specialized stabilizers, and do not cover a comprehensive quantitative evaluation of the multi-enzyme activity of AuPt nanozyme.

To address these limitations, we employed a facile, one-step strategy to synthesize platinum-anchored gold nanozyme (AuPt) with core-shell nanostructure using tannic acid (TA), as both a green reducing and capping agent known for its high antibacterial and antioxidant activities. The resulting phenol-rich surface not only enhances colloidal stability but also contributes to the nanozyme's catalytic performance. The AuPt nanozyme exhibits a broad spectrum of enzyme-like activities, including glucose oxidase (GOD), peroxidase (POD), catalase (CAT), oxidase (OXD), and superoxide dismutase (SOD), positioning it as a multifunctional platform for redox regulation in diabetic wound healing. Importantly, our results indicate that the AuPt nanozymes exhibit cell penetration and intracellular multienzyme activities. Due to the synergistic catalytic activity arising from the combination of gold and platinum, the nanozymes demonstrate glucose oxidation and subsequent catalase activity, which could mitigate hyperglycaemia-associated oxidative stress, resulting in the enhancement of diabetic wound healing (Scheme 1).

2. Result and discussion

2.1. Synthesis and characterization of nanozyme

The AuPt nanozyme was synthesized through a one-step synthesis, utilizing tannic acid as the reducing agent, as depicted in Fig. 1a. The reduction of gold ions (Au^{3+}) by tannic acid initiates the synthesis of gold nanozymes, evidenced by an immediate color transition from yellow to purple. The galloyl-OH groups in tannic acid serve as electron donors, facilitating the reduction of Au^{3+} to Au^0. The observed color change is attributed to the surface plasmon resonance (SPR) of the gold nanoparticles, resulting from their interaction with light as they form and aggregate. In contrast, the platinum precursor mixture did not exhibit a color change upon tannic acid addition, likely due to the distinct reduction potentials of gold and platinum, with gold being more readily reduced as indicated by its higher standard reduction potential (+1.50 V for the Au^{3+}/Au^0 couple) compared to platinum (+0.68 V for the Pt^{4+}/Pt^{2+} couple and + 1.2 V for the Pt^{2+}/Pt^0 couple) [29].

As the reaction progresses, the concentration of Au^0 increases and aggregation starts due to Van der Waals forces until reaching a saturation point, where Au^0 begins to nucleate, forming initial crystal nuclei, which subsequently grow into nanoclusters as additional Au^0 atoms deposit onto the surface of the nuclei, thereby reducing the concentration of Au^0 and resulting in the formation of a stable Au nanozyme. In this process, tannic acid acts as a reducing agent that undergoes self-oxidation, leading to the formation of a quinone. These quinone-derived carbonyl groups act as capping agents and bind to the surface of the formed Au nanozymes primarily through coordination via their carbonyl oxygen atoms and additional stabilization provided by π-electron interactions from the aromatic rings [30]. The initial formation of the gold nanozymes was followed by the deposition of platinum atoms. The presence of quinone carbonyl groups on the surface of gold nanozyme enhances the in situ reduction of platinum ion (Pt^{4+}) over a duration of 4 h at a controlled temperature of 60 °C, resulting in anchoring platinum sites to form gold anchored platinum nanozyme (AuPt), combining the unique functionalities of both metals [31]. This process is accompanied by a color change of the suspension from light

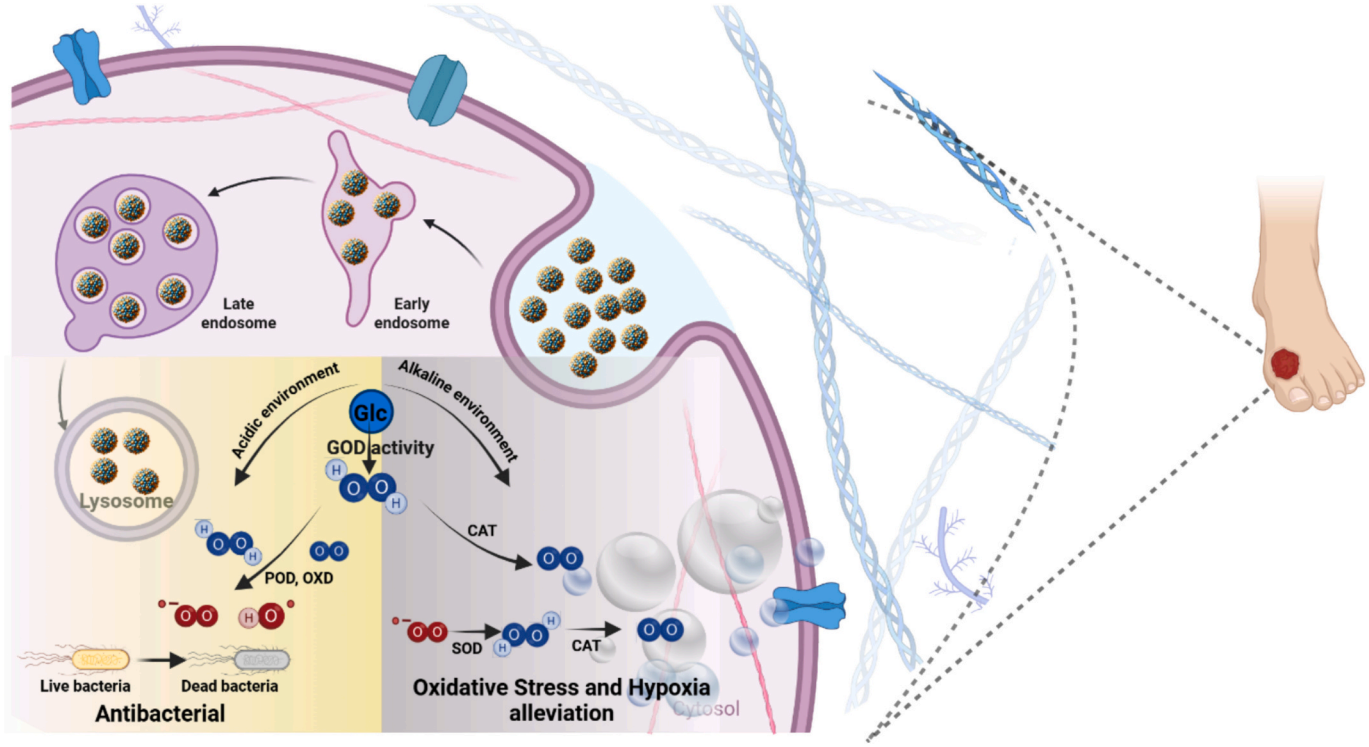

Scheme 1. Schematic illustration of the therapeutic mechanism of AuPt nanozymes in diabetic foot ulcers. The nanozymes catalyze multienzyme-like activities, including the decomposition of H_2O_2 (via catalase and peroxidase-like activity) and scavenging of reactive oxygen species (ROS, via superoxide dismutase-like activity). These activities restore redox balance, reduce oxidative stress, and promote tissue repair, as demonstrated in the diabetic wound healing model.

purple to brown. In addition to acting as a reducing agent, tannic acid forms a phenol–quinone redox layer on the gold surface that facilitates electron transfer and regulates platinum deposition. This interfacial layer promotes charge redistribution between Au and Pt while stabilizing the bimetallic structure through coordination and π–π interactions [32].

The UV–vis absorption spectra revealed distinctive peaks for both the Au and the AuPt nanozymes (Fig. S2). Both Au and AuPt nanozymes displayed the characteristic surface plasmon resonance peak at 530 nm, indicative of gold nanozyme formation (Fig. S2). For the AuPt nanozymes, an additional peak appeared at 255 nm, which corresponded to the platinum deposition on the gold surface, confirming the formation of the bimetallic structure (Fig. S2b).

Dynamic Light Scattering (DLS) and zeta potential results demonstrated no significant difference between the size of Au (34 nm) and AuPt (37 nm) (Fig. S3), as well as the surface charge −23.1 mV for AuPt and 21.4 mV for the Au (Fig. S4), indicating that the Pt deposition has not significantly increased the Au nanozyme diameter. The negative charge is attributed to the tannic acid (TA) capping, which helps stabilize the nanoparticles by providing electrostatic repulsion and preventing aggregation [30]. Moreover, an investigation of the size stability exhibited that both Au and AuPt nanozymes demonstrated size stability for 30 days in BPS at 37 °C due to their negative surface charge, preventing aggregation caused by the electrostatic repulsion (Fig. S5).

Transmission electron microscopy (TEM) images (Fig. 1b) exhibited a spherical morphology for both nanozymes with a similar average size, confirming that the Pt deposition did not change the nanozyme size. Au nanozymes exhibited a well-defined sharp-edge spherical morphology in their outer layer, while Pt anchoring altered the surface morphology to a more fluffy surface. X-ray diffraction (XRD) analysis (Fig. 1c), exhibited distinct peaks that correspond to the crystalline structure of gold (Au) nanozymes. These peaks, precisely positioned at 38.09°, 44.32°, 64.58°, 77.44°, and 81.49°, are attributed to the (111), (200), (220), (311), and (211) planes, respectively, aligning with the standard cubic gold structure (JCPDS No. 04–0784) [33]. Although similar peaks were observed for AuPt nanozymes, the intensity of the diffraction peaks decreased compared to the Au nanozymes, suggesting a slight reduction in crystallinity due to the incorporation of Pt; however, the original crystalline phase was maintained without the formation of separate compounds.

The crystallographic information of the synthesized Au and AuPt nanozymes was further evaluated by selected area electron diffraction (SAED) patterns. The SAED pattern for the Au nanozyme (Fig. 1d) displayed concentric diffraction rings characteristic of a face-centered cubic (fcc) gold structure [34]. For the AuPt nanozyme (Fig. 1e), the SAED pattern also exhibited concentric diffraction rings, indicating that the incorporation of platinum did not disrupt the fcc structure of the gold core. However, a slight reduction in diffraction ring intensity was observed for the AuPt nanozyme compared to the Au nanozyme, consistent with the XRD data, suggesting a slight perturbation in the diffraction intensity due to Pt incorporation.

The high-angle annular dark-field scanning TEM (HAADF-STEM) image (Fig. 2a) showed a consistent distribution of Au and Pt signals across different nanostructures. The mapping images demonstrated the placement of the Pt atoms anchored on the gold nanozyme's exterior regions, confirming the core-shell structure. The nanozymes showed an average Au core diameter of 19.8 ± 3.2 nm and a Pt shell thickness of 3.4 ± 0.5 nm. Additionally, the energy-dispersive X-ray spectroscopy (EDS) (Fig. 2b) revealed the coexistence of Au and Pt signals, indicating the successful formation of the bimetallic structure. To investigate the trace of TA on the nanozymes, FTIR was performed (Fig. 2c). TA spectrum exhibited the characteristic peaks at 3500–3000 cm^{-1} for phenolic -OH groups, at 1698 cm^{-1} for carbonyl stretches in carboxylic esters, at 1614–1443 cm^{-1} for aromatic C═C bonds, at 1183–1120 cm^{-1} for benzene ring vibrations, and at 757 cm^{-1} for aromatic C—H bends [9,35]. In both Au and AuPt spectra, the intensity of phenolic-OH peaks at 3500–3000 and 1345 cm^{-1} was reduced, which could be due to the oxidation of those groups during the reduction reaction. Moreover, the

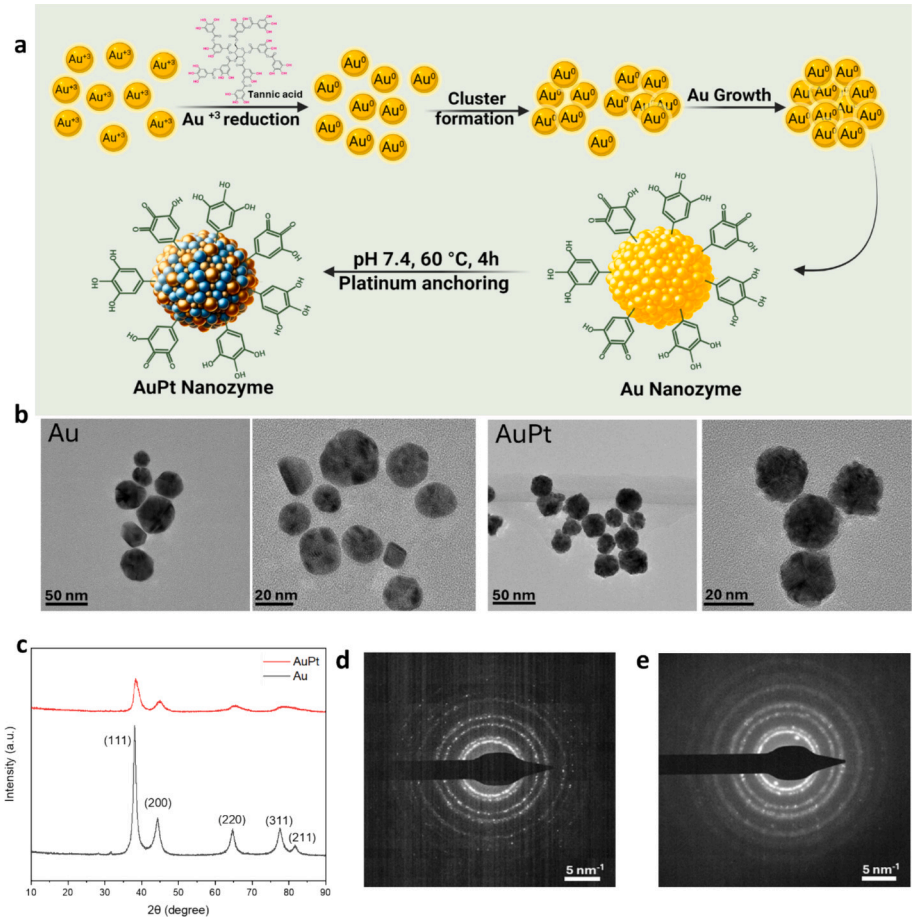

Fig. 1. Preparation and morphology characterization of Au and AuPt nanozyme. a) Schematic illustration of the preparation strategy for AuPt nanozyme, tannic acid (TA) acts as a reducing agent, reducing Au^{3+} to Au^0 and facilitating the formation of gold nanoclusters. The residual carbonyl groups on TA, adsorbed onto the gold surface, subsequently reduce Pt^{4+} ions in situ, forming the bimetallic AuPt structure b) TEM image of Au and AuPt nanozyme. c) XRD patterns of Au and AuPt nanozyme. d) SAED pattern of Au and e) AuPt nanozyme.

presence of a peak at 1615 cm^{-1} in Au and AuPt spectra could be indicative of the o-quinone structure, confirming the oxidation of TA on the nanozyme surface [36].

The surface composition and oxidation states of the Au and AuPt nanozymes were characterized using X-ray photoelectron spectroscopy (XPS). The survey spectrum of AuPt revealed distinct binding energy peaks corresponding to Au 4 f and Pt 4 f, as well as O 1 s and C 1 s regions, confirming the successful formation of AuPt (Fig. 2d, and Table S1). In the high-resolution XPS spectra of AuPt, the O 1 s spectrum presented two distinct components, attributable to metal-oxygen (C—O) and carbonyl (C=O) bonds (Fig. 2e). The deconvoluted C 1 s spectrum peaks indicated two distinct peaks corresponding to carbon-carbon (C—C) bonds, as well as carbon bonded to oxygen (C—O) (Fig. 2f). The O 1 s and C 1 s spectra exhibit the presence of TA residues. Moreover, the deconvoluted Au 4 f spectrum showed two pronounced peaks at approximately 84.24 and 87.94 eV, which can be attributed to the Au 4 f7/2 and Au 4 f5/2 spin-orbit components, indicative of metallic gold (Au^0) states (Fig. 2g). The Pt 4 f spectrum was deconvoluted into four peaks, with peaks at 72.89 and 76.47 eV corresponding to the Pt 4 f7/2 and Pt 4 f5/2 of metallic platinum (Pt^0), and additional peaks at 73.84 and 77.83 eV, which are indicative of Pt^{2+} species, indicating the coexistence of Pt^0 and Pt^{2+} likely due to the formation of a partial oxidation layer [37] (Fig. 2h). Quantitative analysis based on integrated peak areas of the Au 4 f and Pt 4 f regions (Table S1) yielded a surface Pt/Au atomic ratio of approximately 1.5, confirming a Pt-enriched surface consistent with the core–shell morphology observed by HAADF-STEM. Mixed valence states in Pt-based nanozymes have been shown to enhance electron transfer efficiency compared to purely metallic Pt^0, thereby facilitating catalytic redox processes [38].

2.2. Enzyme-mimicking activities of the nanozymes

In vitro multi-enzyme mimicking activities of Au and AuPt nanozymes were investigated. The peroxidase-like (POD) activity of the nanozymes was assessed through a colorimetric assay utilizing 3,3′,5,5′-tetramethylbenzidine (TMB). POD mimic nanozymes catalyze H_2O_2 to form hydroxyl radical (OH•), resulting in the oxidation of TMB with absorbance at 652 nm. AuPt nanozyme exhibited a significantly higher POD activity than Au nanozyme (Fig. 3b). We investigated the concentration-dependent POD activity of Au (5–25 μg/mL) and AuPt (0.05–0.25 μg/mL), by measuring the absorbance at 652 nm as a function of time. The specific activity (SA) was measured from the change in the absorbance per minute (Fig. S6, S7). Both Au (Fig. S6a) and AuPt (Fig. S7a) nanozymes exhibited a concentration-dependent POD activity. The AuPt nanozyme exhibited a SA of 108 U/mg (Fig. S7b), which was more than 100 times higher than the SA of the Au nanozyme (0.7 U/mg) (Fig. S6b). Furthermore, we performed a kinetic study, and the Michaelis–Menten curves were obtained for both Au (2.5 μg/mL) and AuPt (0.25 μg/mL) where the nanozyme concentration was adjusted to ensure measurable activity within a suitable TMB range. (Fig. 3c). Au nanozyme showed a Michaelis constant (K_m) and maximum reaction rate (V_{max}) of 2.6 mM and 2.38 μM/min, respectively, while AuPt nanozyme exhibited K_m and V_{max} of 0.15 mM and 22.96 μM/min, revealing that the Pt anchoring could introduce the POD activity of the

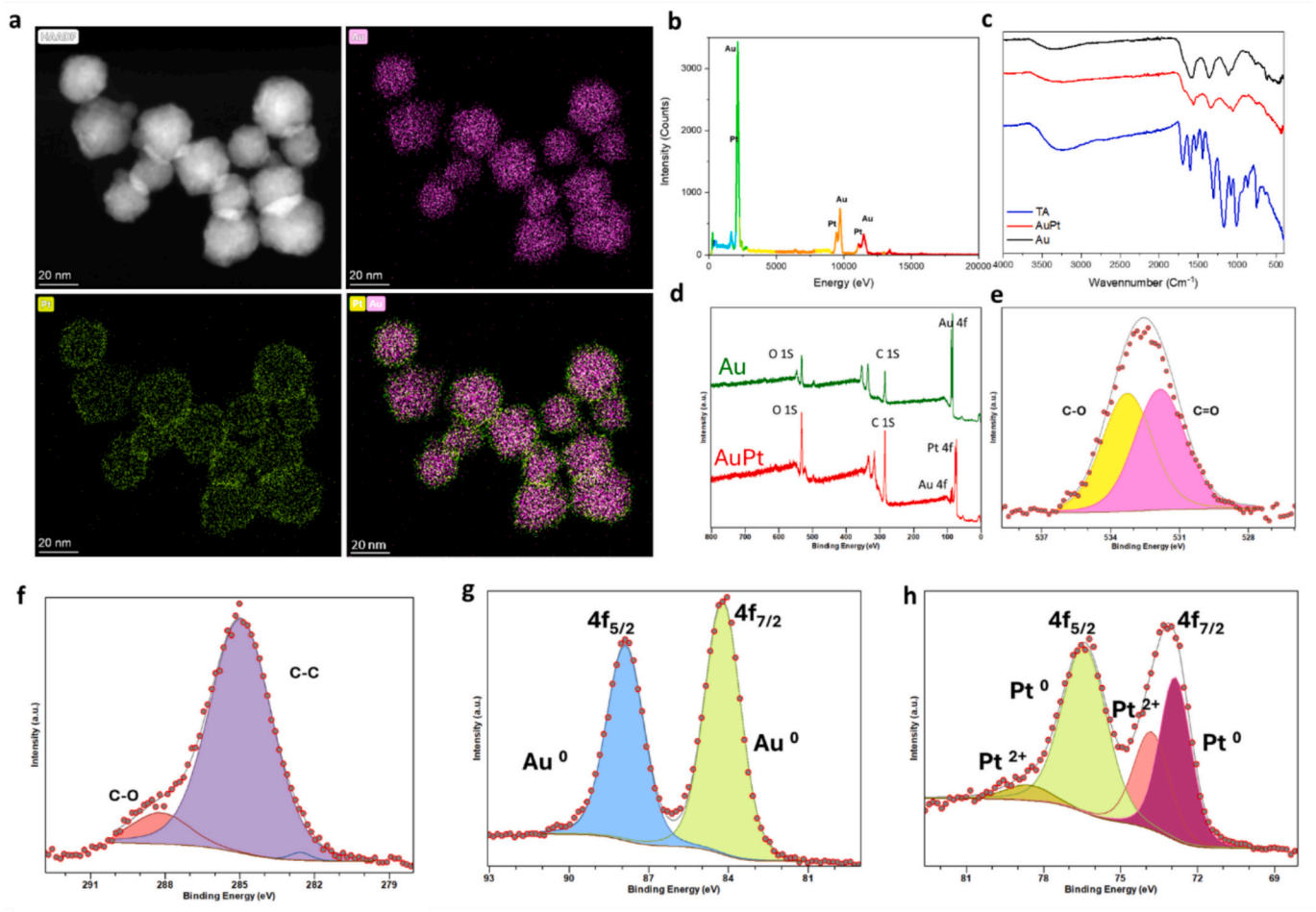

Fig. 2. Structural characterization of Au and AuPt nanozyme. a) High-angle annular dark-field scanning TEM (HAADF-STEM) image of AuPt nanozyme. b) Energy-dispersive X-ray spectroscopy (EDS) of AuPt nanozyme. c) FTIR spectra of Au, AuPt, and TA. d) XPS spectra of Au and AuPt. e) High-resolution spectra of O 1 s, f) C 1 s, g) Au 4 f, and h) Pt 4 f.

nanozyme. Furthermore, the POD activity of the natural horseradish peroxidase (HRP) enzyme was tested (Fig. S8). The tested horseradish peroxidase (HRP, lyophilized, powder, ~150 U/mg) exhibited a SA of 147 U/mg (Fig. S8b) and K_m and V_{max} of 0.35 mM and 7.79 μM/min (Fig. S8c), respectively, indicating that the developed AuPt nanozyme showed POD specific activity comparable to HRP. Representative kinetic parameters and specific activity of previously reported POD nanozymes have been summarized in Table S6. The AuPt nanozyme exhibited a high specific activity (108 U/mg) and a low K_m (0.13 mM), placing it in the upper range of reported systems—comparable to ACPCAH (120 U/mg) and Fe single-atom nanozymes (103.8 U/mg). The results highlight the strong catalytic efficiency and substrate affinity of our nanozyme, achieved via a simple one-step synthesis. The superior POD activity of AuPt possibly arises from Pt active sites working in concert with the TA-derived phenol–quinone redox layer (present on both Au and AuPt). Tannic acid forms a phenol–quinone redox layer that facilitates interfacial electron transfer and maintains catalytic turnover, consistent with previous reports on polyphenol-stabilised gold nanozymes [30].

Additionally, we evaluated the impact of pH on the POD activity of AuPt, showing pH-dependent POD activity with a maximum relative activity at pH 4. Increasing the pH to physiological pH significantly decreases the POD activity of AuPt, which drops below 10%, while HRP showed optimum activity at pH 6 (Fig. S9). While chronic wounds maintain an alkaline environment, transient acidity may occur during the early healing phase or in areas of intense inflammation. Under acidic conditions, the enhanced POD activity of AuPt may contribute to antibacterial effects via ROS generation [39].

In the literature, the POD activity of nanozymes is often reported based on only the active sites of the nanoparticles. However, it is crucial to consider the entire nanoparticle structure, including the ballast, which can significantly affect the overall catalytic performance. Robert et al. highlighted that the catalytic efficiency of Fe_3O_4 nanoparticles, which was initially reported to have significant POD activity, was later found to be marginal when the total weight of the nanoparticles was considered, instead of considering only the active site and ignoring the inactive parts of the nanoparticles that contribute to their total mass. They recalculated the POD activity based on the whole mass of nanozyme required to oxidize 1 g of TMB and found that 36.2 g of Fe_3O_4 nanoparticles are required to oxidize 1 g of TMB, which is more than 36-fold the weight of the substrate. This substantial mass requirement clearly indicates that Fe_3O_4 cannot be considered an effective catalyst under these conditions.

Consequently, the calculation of nanozyme activity should not be biased by considering only the number of "catalytic sites" in relation to the total particle mass. This approach is similar to that used for natural enzymes, which contain inactive portions contributing to their total weight [40]. In this regard, we calculated the amount of each catalyst required to oxidize 1 g of TMB, comparing Au and AuPt nanozymes to natural HRP (Fig. S10). Our results showed that 0.86 g of HRP is required to oxidize 1 g of TMB, indicating a 0.86 wt% with respect to the substrate (Fig. S10c). For the Au, 176.44 g is required to oxidize 1 g of TMB (Fig. S10d). In contrast, only 0.995 g of AuPt is required to oxidize

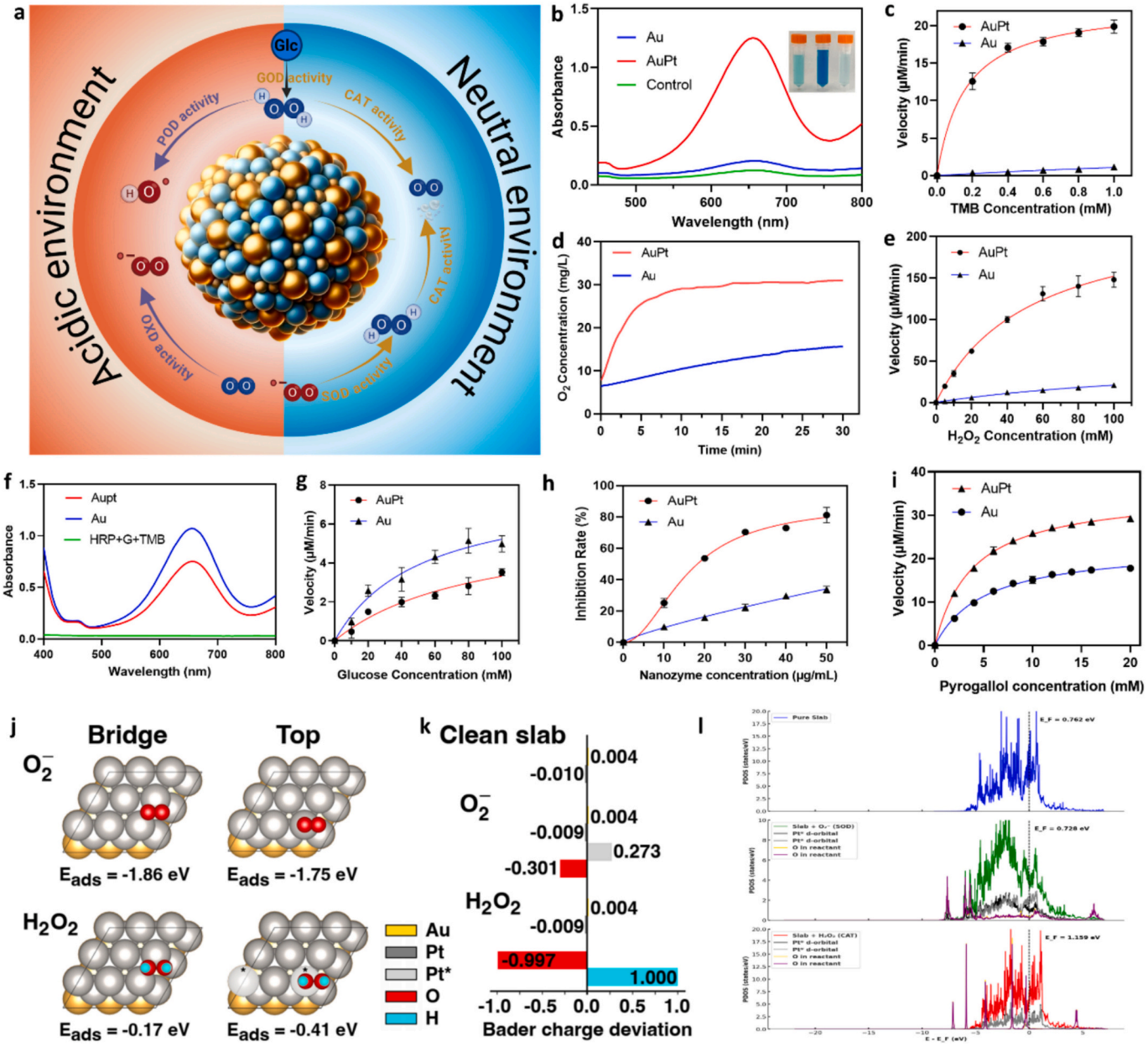

Fig. 3. Multi-enzyme-like activities of Au and AuPt nanozymes. a) Schematic illustration of the multi-enzyme activities of AuPt nanozymes, including peroxidase, oxidase, catalase, and superoxide dismutase-like activity across varying pH levels. b) POD-like activity of Au and AuPt nanozyme. c) Michaelis-Menten curves of POD-like activity of Au and AuPt nanozyme. d) Time-dependent oxygen generation showing CAT-like activity of Au and AuPt nanozymes. e) Michaelis-Menten curves of the CAT-like activity of Au and AuPt nanozyme. f) GOD-like activity of Au and AuPt nanozyme. g) Michaelis-Menten curves of GOD-like activity of Au and AuPt nanozyme. h) Concentration-dependent inhibition rate of pyrogallol autoxidation by Au and AuPt nanozyme. i) Michaelis-Menten curves of SOD-like activity of Au and AuPt nanozyme. j) Adsorption energies of superoxide (O_2^-) and hydrogen peroxide (H_2O_2) on AuPt nanozyme surfaces. k) Bader charge deviations for the most stable adsorption configurations of O_2^- (bridge) and H_2O_2 (top) on the AuPt slab. The charge deviations are reported with respect to the nominal charge of the different species. *For* H_2O_2 (top) on the AuPt slab, *the Pt atom* adjacent to the H_2O_2 molecule (Pt*) has a very different deviation compared to all other Pt atoms. l) Projected Density of States (PDOS) analysis for the clean AuPt surface, and upon adsorption of O_2^- (SOD-like) and H_2O_2 (CAT-like). Top: Clean slab showing sharp d-band features centered below the Fermi level. Middle: Upon adsorption of O_2^-, Pt d-orbitals (black/gray) exhibit a downward shift, indicating electron donation to the reactive species and stabilizing the adsorbate.
Bottom: Adsorption of H_2O_2 induces only minor perturbations in the d-band, reflecting weaker electronic interaction and easier desorption.

1 g of TMB, indicating a 0.995 wt% with respect to the substrate (Fig. S10e). Our results align with Robert and Meunier's assertion that evaluating the total nanoparticle structure and weight is crucial for accurately determining catalytic capabilities [40]. The higher POD activity of AuPt arises from its Pt-rich surface and mixed Pt^0/Pt^{2+} states, which facilitate electron transfer and •OH radical generation. The high specific activity and kinetic parameters of the AuPt nanozyme indicate its potential as a nanozyme catalyst, whereas the Au, with its significantly lower activity, may not be considered a POD nanozyme.

Next, we investigated the nanozymes' CAT-like activity. CAT-like nanozymes are known for their ability to decompose H_2O_2 into O_2. The CAT activity of the nanozyme was evaluated by assessing the time-dependent generation of dissolved oxygen and its ability to scavenge H_2O_2. As shown in Fig. 3d, the AuPt nanozyme showed higher generated dissolved oxygen after 10 min (30 mg/L) compared to the Au nanozyme (15 mg/L after 30 min), revealing the enhancement of CAT activity after

Pt deposition.

Moreover, the amount of bubbles produced by AuPt nanozyme compared to Au nanozyme indicates the significantly higher CAT activity caused by Pt atom deposition (Fig. 11a). Similar to POD activity, the concentration-dependent CAT activity of Au (Fig. S11b) and AuPt (Fig. S12a) nanozyme was determined, and the CAT SA of Au nanozyme was 6.5 U/mg (Fig. S11c). In comparison, the AuPt nanozyme exhibited a CAT SA of 96.6 U/mg (Fig. S12b), indicating the enhancement of CAT activity. Moreover, the Michaelis–Menten kinetic study at different concentrations of H_2O_2 and a fixed concentration of nanozymes (3 μg/mL) was performed. The results demonstrated a K_m and V_{max} of 162.2 mM, and 54.55 μM/min for the Au nanozyme, while the AuPt nanozyme exhibited a K_m and V_{max} of 52.69 mM, and 232.1 μM/min (Fig. 3e). Additionally, the ability of the nanozyme to scavenge H_2O_2 was determined by monitoring the absorbance at 240 nm (Fig. S13), and the result confirmed a higher decomposition rate of H_2O_2 by AuPt compared to Au nanozyme (Fig. S13). Furthermore, the kinetic investigation of natural catalase enzyme (50 ng/mL) at different H_2O_2 concentrations exhibited a K_m of 8.5 mM and a V_{max} of 283.5 μM/min (Fig. S14a). Representative CAT-like nanozyme activities are summarized in Table S7. The AuPt nanozyme exhibited a high specific activity of 96.6 U/mg, outperforming previously reported AuPtCo nanozymes (27.1 U/mg) and even some single-atom systems, such as Ru (16.6 U/mg) and Pd (2.39 U/mg). Notably, despite using a similar AuPt composition, the superior activity of our system may be attributed to the phenolic-rich surface introduced by tannic acid, which could enhance electron transfer and catalytic efficiency.

The impact of pH on the CAT activity of the nanozyme and the natural enzyme was also investigated (Fig. S14b). For the AuPt nanozyme, the CAT activity increased as the pH shifted from acidic to alkaline conditions. The nanozyme exhibited optimal CAT activity at pH 10, indicating enhanced stability and performance in alkaline environments, while the natural enzyme demonstrated optimum activity at pH 7, and its activity diminished beyond pH 7. The enhanced CAT-like activity of the AuPt nanozyme at alkaline pH is particularly beneficial for chronic diabetic wounds, which often exhibit an alkaline environment (pH 7.2–9.0) that contributes to oxidative stress and impedes healing [41].

The glucose oxidase (GOD) mimic activity of the nanozyme was measured by its ability to oxidize glucose to generate H_2O_2. Similar to the peroxidase (POD) activity assay, the TMB assay was employed in the presence of HRP to ensure that the generated H_2O_2 led to the oxidation of TMB. According to the absorbance at 652 nm, which corresponds to oxidized TMB (OxTMB), the Au nanozyme exhibited higher GOD activity compared to the AuPt nanozyme (Fig. 3f). Specifically, the Au nanozyme demonstrated 40% higher relative activity than the AuPt nanozyme (Fig. S15). This difference in GOD activity can be attributed to the inherent characteristics of gold (Au) nanozyme, which mimic the activity of natural glucose oxidase (GOx) enzymes via a two-step reaction mechanism for glucose oxidation, similar to natural GOx, involving the glucose dehydrogenation followed by reduction of O_2 to H_2O_2. In contrast, platinum (Pt) and other noble metals, while capable of catalyzing glucose dehydrogenation, preferentially produce H_2O rather than H_2O_2 [42]. Therefore, when Pt is deposited on Au nanoparticles to form AuPt nanozymes, the overall GOD activity is reduced compared to pure Au nanozymes at the same concentration. Moreover, the Michaelis–Menten kinetic study at different glucose concentrations and fixed concentration of nanozymes (5 μg/mL) was performed (Fig. 3g). The results demonstrated a K_m of 51.3 mM and a V_{max} of 7.8 μM/min for Au nanozyme, while the AuPt nanozyme exhibited a K_m of 85.7 mM and a V_{max} of 6.1 μM/min, indicating the higher apparent affinity of Au nanozyme.

The SOD mimic activity of nanozymes was investigated using the pyrogallol autoxidation inhibition assay, which measures the ability of nanozymes to reduce the spectrophotometrically detectable formation of purpurogallin at 325 nm, which results from the autoxidation of pyrogallol in alkaline conditions. A lower absorbance at 325 nm indicates a stronger inhibition of the superoxide radicals ($O_2^{\cdot-}$), and the IC_{50} value, which represents the concentration required to reduce the rate of purpurogallin formation by 50%, is used to quantify SOD activity [43]. The AuPt nanozyme exhibited a lower increase in the absorbance at 325 nm compared to the Au nanozyme and the control (Fig. S16a). The autoxidation rate was determined from the slope of the linear region of the curve (0–120 s) and was reduced by 46% in the AuPt group compared to the control, and by 30.1% compared to the Au nanozyme. Both nanozymes demonstrated a concentration-dependent SOD activity (Fig. S16b,c) with the calculated IC_{50} of 70.1 and 17.3 μg/mL for Au and AuPt, respectively (Fig. 3h). The Michaelis–Menten kinetic study at different concentrations of pyrogallol (0–20 mM) and a fixed concentration of nanozymes (25 μg/mL) was performed. The results demonstrated a K_m of 5.1 mM and a V_{max} of 22.8 μM/min for Au nanozyme, while the AuPt nanozyme exhibited a K_m of 3.8 mM and a V_{max}, of 35.33 μM/min (Fig. 3i). All enzyme-like kinetic parameters (Km, Vmax, kcat, and kcat/Km) for POD, CAT, GOD, and SOD activities of Au, AuPt, and corresponding natural enzymes, calculated based on ICP-determined metal concentrations, are summarized in Tables S2–S5. The enzyme activity of the nanozymes in complex biological fluids was not evaluated in this study and should be considered in future investigations.

2.3. Computational study

To validate the structural and catalytic properties of the AuPt core-shell nanozyme, density functional theory (DFT) calculations were conducted. The system is modeled using a slab consisting of 5 layers of Au, mimicking the core, and two layers of Pt. The geometry was optimized using Quantum ESPRESSO by relaxing atomic positions and lattice parameters until force convergence was achieved. All technical details are given in the Methods section. The simulated XRD pattern (Fig. S17a) for the optimized AuPt nanozyme model reveals two prominent peaks in the 2θ range at ~38° and ~ 44°, corresponding to the (111) and (200) planes of Au and Pt, respectively. These results align closely with experimental XRD data (Fig. 1c).

The core Au and shell Pt atoms both retain their FCC lattice configuration with minimal perturbations.

We also investigated the adsorption energy (E_ads) of H_2O_2 and O_2^- on the Pt surface of our model, mimicking the shell part of AuPt core-shell nanozyme. There are two adsorption sites: one on top of a Pt atom and one between two Pt atoms, referred to as bridges. The calculated values of E_ads are reported in Fig. 3j. The most stable configuration for O_2^- is the bridge one (with E_ads = −1.86 eV), while it is the top one for H_2O_2 (with E_ads = −0.41 eV). The strongly negative value of E_ads for O_2^- highlights the nanozyme's ability to effectively bind and stabilize O_2^-. In contrast, the moderately negative value of E_ads for H_2O_2 indicates a possible binding but with easy product release. These calculations correlate with the experimental observations, namely a low K_m and V_{max} for SOD activity and a high K_m and V_{max} for CAT activity.

Bader charge analysis was conducted for the two most stable configurations (Fig. 3k) to investigate the underlying mechanisms in terms of electron redistribution upon adsorption. Here, we report the computed charge deviations with respect to the nominal charge of the different species. For the pure slab (AuPt), the charge deviation of Au is approximately +0.004 (metallic Au^0) while that of Pt is −0.010 (metallic Pt^0). These charge deviations indicate that these atoms are in a neutral metallic state. For the O_2^- adsorption (bridge), the charge deviation for Au remains at +0.004, that of Pt for most of the atoms is −0.009, but it goes to +0.273 for the two atoms close to the O atoms (Pt*), and that of O is −0.301. We thus observe that (i) gold does not have any active participation in the stabilization of reactive species, (ii) two platinum atoms donate electrons to stabilize the adsorbed O_2^- species, and (iii) oxygen receives electrons from Pt. For the H_2O_2 adsorption (top), the charge deviations of Au remain at +0.004, and that of Pt is −0.009, while those of O and H are −0.997 and + 1.000,

respectively. In this case, we see that (i) gold and platinum are essentially unchanged, and (ii) oxygen receives electrons from hydrogen.

The projected density of states (PDOS) (Fig. 3l) was also examined to understand how the local electronic structure of the surface, particularly the Pt d-orbitals, responded to reactant adsorption. In the case of SOD-like activity, the PDOS showed broadening and shift in the Pt d-states, indicating electron donation to the adsorbed species. This is consistent with the highly negative adsorption energy (Fig. 3j) and the Bader charge analysis (Fig. 3k) and explains the slower product release observed experimentally. In contrast, CAT-like activity induced only minor changes in the d-band. The Pt d-states remained mostly intact, suggesting weaker orbital overlap and limited charge transfer. This behavior correlates with less negative adsorption energy, minimal Bader shifts, and the experimentally observed faster catalytic turnover (higher V_{max}).

To complement the adsorption and electronic structure results, reaction energy diagrams for the SOD-like (O_2^- dismutation) and CAT-like (H_2O_2 decomposition) reactions on the AuPt surface were further examined based on the DFT total energies of fully optimized configurations. For each process, the initial state (IS), a sequence of surface-stabilised intermediates (Int1–Int3), and the final desorbed products (FS) were identified. The full pathways and energy profiles are provided in the Supplementary Information (Fig. S17b–d).

For the SOD-like pathway, sequential protonation and surface-assisted O—O bond cleavage generate $HOO^\bullet$ intermediates that are strongly stabilised on Pt, resulting in a highly exergonic reaction energy ($\Delta E = -7.83$ eV). This strong thermodynamic driving force is consistent with the large negative adsorption energy of O_2^-, the substantial charge transfer revealed by Bader analysis, and the pronounced d-band modulation observed in PDOS.

In contrast, the CAT-like pathway proceeds through $HO_2^\bullet$ and $OH^\bullet$ species generated from H_2O_2 dissociation. These intermediates are less strongly stabilised, and the overall reaction exhibits a smaller exergonic reaction energy change ($\Delta E = -2.84$ eV), reflecting weaker orbital overlap and more limited charge redistribution. This aligns with the moderate adsorption energy of H_2O_2 and the minimal perturbation of Pt d-states, consistent with the experimentally observed faster turnover and easier product release.

2.4. In vitro cell studies

The in vitro cytotoxicity of Au and AuPt nanozymes was determined using fibroblast cells (3 T3 cell line) by CellTiter 96® AQ_{ueous} One Solution Cell Proliferation Assay (MTS). At the 24-h time point, both Au and AuPt nanozymes exhibited high cell viability across all tested concentrations (> 80%), indicating minimal cytotoxicity (Fig. 4a). However, when the exposure duration increased to 48 h (Fig. 4b), a decline in cell viability was observed for Au at high concentrations (50 and 100 μg/mL), whereas the AuPt maintained higher levels of cell viability at these same concentrations. Extended incubation for 7 and 14 days did not result in additional cytotoxicity for the nanozymes, with sustained cell viability observed across all tested concentrations (Fig. S18).

Then, based on the MTS assay result, a live/dead assay was performed at a concentration of 25 μg/mL for two days (Fig. 4c). Hoechst and ethidium homodimer-1 (EthD-1) were used to stain nuclei in intact or damaged cells, respectively. Nearly no cell exhibited EthD-1 signal, confirming the good cell viability upon incubation with AuPt. The lower cell viability of Au nanozyme could possibly be due to its high GOD activity, which can catalyze glucose oxidation, which will consume oxygen and generate H_2O_2, resulting in reduced cell viability [21]. However, AuPt nanozyme with relatively lower GOD and higher CAT activity compared to the Au nanozyme, can effectively catalyze the generated H_2O_2 to O_2, and thus protect the cells against oxidative stress. To validate this hypothesis, we evaluated the intracellular ROS and O_2 levels of fibroblast cells treated with both Au and AuPt at a concentration of 50 μg/mL for 48 h. The intracellular ROS level was investigated by 2′,7′-dichlorodihydrofluorescein diacetate (DCFH-DA) probe (Fig. 4d). The results showed a higher ROS accumulation in cells treated with the Au nanozyme compared to both the control and the AuPt-treated cells. This observation aligns with the predicted higher GOD activity of the Au nanozyme, which facilitates the production of H_2O_2, subsequently leading to increased ROS levels, while the ROS levels in cells treated with the AuPt nanozyme were comparable to the untreated control group.

The intracellular oxygen levels were assessed using $[Ru(dpp)_3]^{2+}Cl_2$ (RDPP), a phosphorescent probe whose light emission is highly sensitive to quenching by oxygen. The fluorescence microscopy images (Fig. 4e) revealed that cells treated with the Au nanozyme displayed higher red fluorescence intensity compared to AuPt and the control, indicative of low intracellular oxygen levels, validating the O_2 consumption by Au nanozyme during the glucose oxidation. The results underscore the capability of the AuPt nanozyme to mitigate oxidative stress caused by Au effectively, thereby enhancing cell viability and suggesting its suitability for applications where oxidative stress is a critical factor.

Moreover, a cell migration assay was performed to investigate the effect of Au and AuPt nanozymes on wound healing. Neither Au nor AuPt groups displayed any delay in migration, with gaps being filled within 24 h (Fig. 4f). Quantitative analysis shows no significant difference in wound closure among the nanozymes compared to the control, demonstrating that both Au and AuPt nanozyme treatments did not negatively affect cell migration, supporting their biocompatibility and lack of adverse effects on wound healing (Fig. 4g).

Next, we investigated the protective effect of nanozymes against exogenous H_2O_2 damage (Fig. 4h). The results indicated that AuPt nanozyme could effectively protect 3 T3 cells against ROS damage when H_2O_2 was added to the culture medium up to 1 mM for 8 h. In contrast, cell viability in the control and Au groups decreased at concentrations higher than 0.2 mM. The result demonstrated that the AuPt nanozymes effectively scavenge ROS under physiological conditions, primarily due to their dominant CAT activity compared to POD activity at physiological conditions (pH 7.4), which may contribute to protection of cells from oxidative stress-induced damage.

Then, 0.1 mM H_2O_2 was employed to induce oxidative stress, and the therapeutic effect of nanozymes on alleviating oxidative stress was studied. As shown in the fluorescent microscopy images (Fig. 5a), both the Au and control groups exhibited significant green fluorescence, indicating the intracellular ROS level, while AuPt-treated cells demonstrated markedly decreased green fluorescence [44]. Additionally, investigating the intracellular O_2 level (Fig. 5b), demonstrated that AuPt exhibited the weakest red fluorescence compared to the control and Au groups upon incubation with H_2O_2, revealing effective H_2O_2 catalyzing and O_2 generation, suggesting enhanced intracellular oxygen availability under oxidative stress conditions.

We further investigated the intracellular superoxide ion ($O_2^{\bullet-}$) to determine the intracellular SOD activity of Au and AuPt nanozyme (Fig. 5c). $O_2^{\bullet-}$ was induced using menadione as a ROS inducer, and the dihydroethidium (DHE) probe was employed as a reporter. The DHE probe, upon oxidation by $O_2^{\bullet-}$, forms ethidium, which intercalates with DNA and emits red fluorescence. Both Au and AuPt nanozyme groups exhibited less red fluorescence signal compared to the control, as well as a gradual reduction in the red fluorescence with increasing incubation time to 2 h, demonstrating consumption of $O_2^{\bullet-}$, consistent with the SOD-like activity.

To evaluate the effects of Au and AuPt nanozymes on fibroblast cell morphology, bright-field microscopy images were analyzed (Fig. 5d). The images reveal that neither type of nanozyme induced any significant morphological alterations in the fibroblast cells compared to the control group. Cells retained their typical elongated and spread-out morphology, with intact cellular structures, indicating that the nanozymes are biocompatible and do not exert cytotoxic effects. In the zoomed-in images of cells treated with Au and AuPt nanozymes, dark spots were observed near the nuclear region; similar features are also

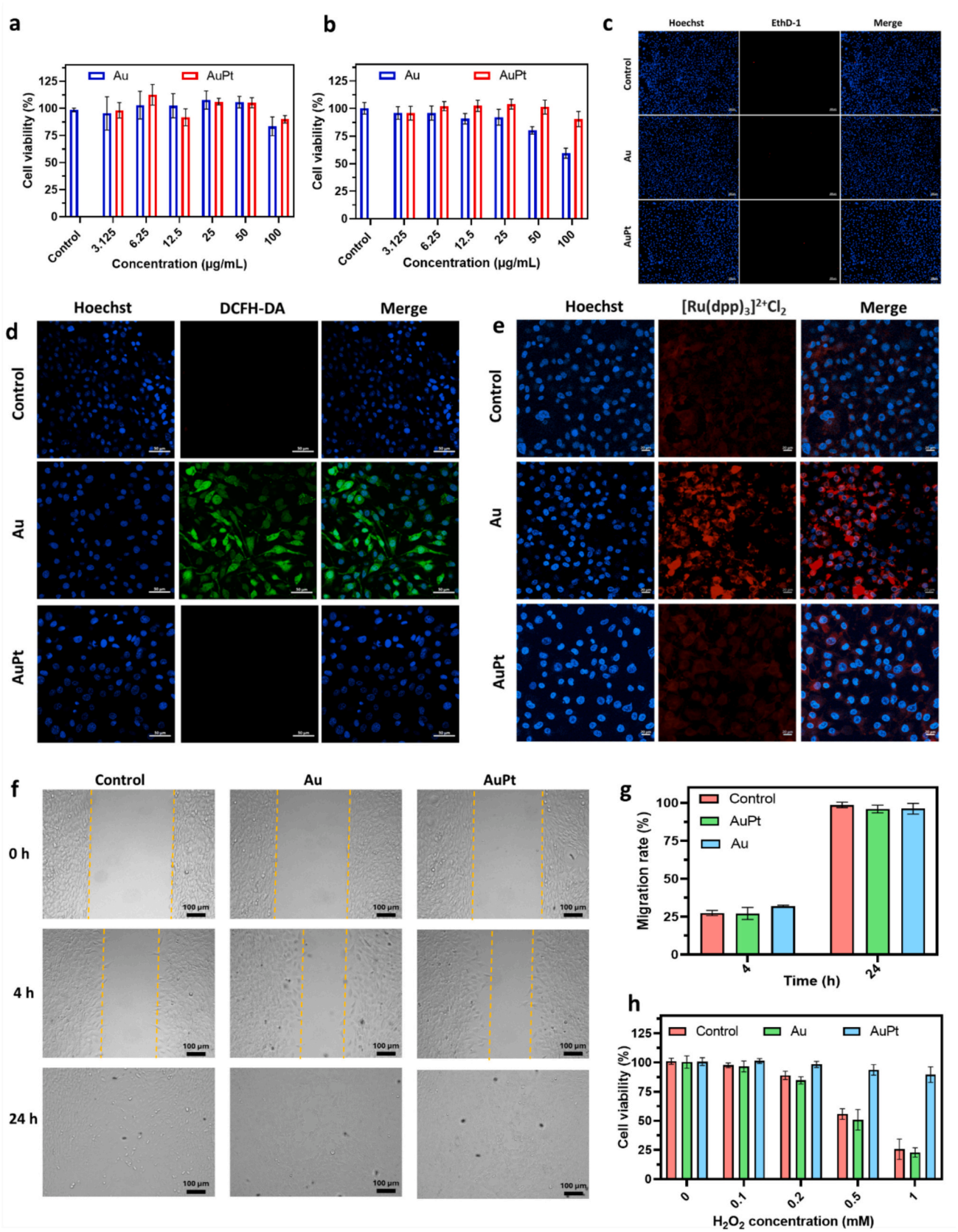

Fig. 4. In vitro studies of 3 T3 cells treated with nanozymes. a) Cell viability of 3 T3-L1 cells treated with Au and AuPt nanozyme with different concentrations (0–100 μg/mL) after 24 (a) and 48 h (b). c) Live/dead analysis of 3 T3-L1 cells treated with Au and AuPt nanozyme (25 μg/mL) after 48 h. d) Intracellular ROS level of 3 T3-L1 cells treated with Au and AuPt nanozyme (50 μg/mL) after 24 h. e) Intracellular O_2 level of 3 T3-L1 cells treated with Au and AuPt nanozyme (50 μg/mL) after 24 h. f) Photograph of the cell migration assay at 0, 4, and 24 h in different treatment groups. g) Quantitative analysis of cell migration of 3 T3-L1 cells treated with Au and AuPt nanozyme after 24 h. h) Protective effect of nanozymes against exogenous H_2O_2 damage.

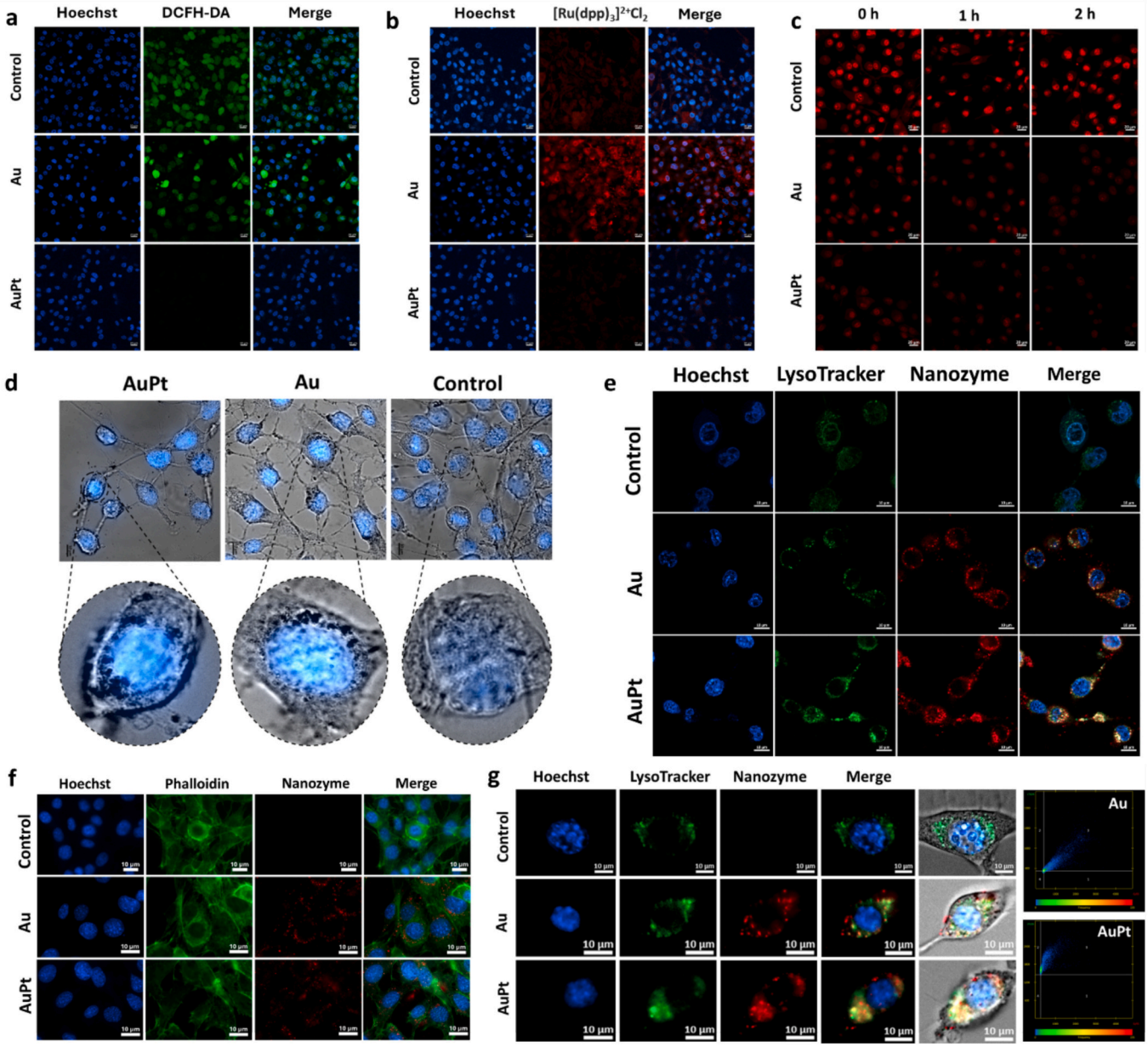

Fig. 5. In vitro intracellular activity and internalization of the nanozymes. a) Intracellular ROS level of 3 T3-L1 cells in the presence of H_2O_2 (0.1 mM) treated with Au and AuPt nanozyme (25 μg/mL). b) Intercellular O_2 level of 3 T3-L1 cells in the presence of H_2O_2 (0.1 mM) treated with Au and AuPt nanozyme (25 μg/mL). c) Intracellular superoxide level of 3 T3-L1 cells in the presence of menadione (50 μM) treated with Au and AuPt nanozyme (25 μg/mL). d) Morphology of 3 T3-L1 cells treated with Au and AuPt nanozyme. e) Confocal laser scanning microscopy images of 3 T3-L1 cells showing the cellular uptake and co-localization of Cy5.5-conjugated Au and AuPt nanozymes with the lysosomes. f) Confocal laser scanning microscopy images of fibroblast 3 T3 cells showing the cellular uptake and interaction of Cy5.5-conjugated Au and AuPt nanozymes with the cytoskeleton. g) Single-cell colocalization analysis.

seen in untreated cells, making their internalization interpretation uncertain. Given the limitations of bright-field imaging, further confirmation was obtained through fluorescently labeled nanozymes. For this purpose, fibroblast cells were incubated with Cy5.5-labeled nanozymes for 24 h, and their internalization was investigated using confocal laser scanning microscopy (CLSM). The nuclei were stained with Hoechst (blue), and lysosomes with LysoTracker (green). In the control group, the cells exhibited clear nuclei and lysosomal staining without any red fluorescence. In contrast, cells treated with Au, and AuPt nanozymes showed distinct red fluorescence, confirming their internalization and co-localization with lysosomes, as demonstrated by the overlap of green and red signals (Fig. 5e). Additionally, to investigate the interaction between nanozymes and the cytoskeleton, cells were stained with Alexa Fluor™ 488 Phalloidin, which selectively binds to F-actin (Fig. 5f). The confocal images revealed the cytoskeletal arrangement, showing clear visualization of actin fibers (green) and their interaction with the internalized nanozymes (Cy5.5, red). The merged images demonstrated that the nanozymes were predominantly located around the nuclei (Hoechst, blue) and along the actin filaments, indicating co-localization of nanozymes with the cytoskeletal within the cellular architecture.

Moreover, single-cell colocalization analysis (Fig. 5g), showed a significant overlap between the Cy5.5-labeled nanozymes (red) and lysosomes (green) signals. For the Au nanozyme, the Pearson correlation coefficient was found to be 0.759, with a Manders' colocalization coefficient of 0.875. The weighted colocalization coefficients were 0.999 for Cy5.5 and 0.681 for LysoTracker, highlighting a strong correlation between the nanozymes and lysosomal compartments. Similarly, the AuPt nanozymes showed substantial co-localization within lysosomes. The

Pearson correlation coefficient was 0.896, and the Manders' colocalization coefficient was 0.948. Weighted colocalization coefficients were 0.951 for Cy5.5 and 0.827 for LysoTracker, suggesting a high degree of overlap between the nanozymes and lysosomal markers. The results suggest that both Au and AuPt nanozymes are effectively internalized by fibroblast cells and predominantly localize within lysosomal compartments, following a similar endocytotic pathway, consistent with previous studies that demonstrated that gold nanoparticles are typically internalized via clathrin-mediated endocytosis, eventually localizing to lysosomes for degradation or processing [45].

As fluorescence microscopy is bound by physical limits, such as spatial resolution and the fact that only the fluorophore, and not the nanozymes themselves, can be observed, and since surface labelling (Cy5.5) can alter nanozyme properties, we further characterized nanozyme internalization using high-resolution Scanning Transmission Electron Microscopy (STEM) (Fig. 6). STEM images of fibroblast cells treated with Au and AuPt nanozymes (24 h), revealed their localization within well-defined membrane-bound intracellular compartments, consistent with multivesicular bodies (MVBs) or lysosomes (Fig. 6, yellow arrowheads). Control fibroblasts also exhibited the presence of multi-vesicular bodies with the same general appearance, size, and number, suggesting that nanoparticle incubation does not lead to a clear modification of cytoplasmic organization or organelle distribution.

Au nanozymes appeared as larger aggregates compared to the AuPt nanozymes, which tended to form smaller clusters within the compartments. Smaller AuPt clusters may enhance their catalytic efficiency due to greater surface area exposure, while larger aggregates of Au nanozymes may reduce their interaction dynamic within the cell.

The internalization of the nanozymes and their subsequent multivesicular bodies/lysosomal localization suggests that nanozymes follow a typical uptake pathway involving clathrin-mediated endocytosis (CME), leading to their sequestration in lysosomes (Fig. 6d). Moreover, a computational study has demonstrated that clathrin assembly facilitates the internalization of nanoparticles, including gold nanoparticles (AuNPs), with size and shape playing crucial roles in the process. For instance, spherical AuNPs are effectively internalized via CME, where clathrin forms a cage around the nanoparticles, enabling their uptake and subsequent trafficking within cells [46].

Furthermore, the observation of multivesicular bodies containing nanozymes supports the hypothesis that these nanozymes could contribute to the regulation of cellular responses to oxidative stress. The AuPt nanozymes, in particular, may exhibit enhanced CAT and SOD activities within these compartments, potentially mitigating oxidative stress in intracellular vesicles involved in ROS processing. The dynamic interaction between nanozymes and lysosomal vesicles may thus provide a protective mechanism against cellular damage by efficiently converting harmful ROS, such as hydrogen peroxide, into oxygen, thereby alleviating oxidative stress and promoting cell survival.

In vitro antibacterial performance of nanozymes.

The antibacterial activity of nanozymes, attributed to their POD activity, which generates ROS, was investigated against *Escherichia coli* (*E. coli*) and *Staphylococcus aureus* (*S. aureus*) as Gram-negative and Gram-positive bacteria strains, respectively. The bacteria were treated with nanozymes (25 μg/mL) in the presence and absence of H_2O_2, the substrate for POD, at physiological conditions (pH 7.4). The antibacterial activity was assessed by the plate colony-counting method. To minimize toxicity to mammalian cells while maintaining antibacterial efficacy, a low concentration of H_2O_2 (0.5 mM) was used, as higher concentrations can be harmful due to interactions with the negatively charged lipid membrane and the potential to induce apoptosis [47]. H_2O_2 was applied for 24 h at a 0.5 mM concentration, a level at which AuPt nanozymes were shown to still protect mammalian cells from oxidative damage (Fig.. 4h). The results showed no significant reduction in colony numbers between the control group (treated with PBS) and nanozyme (Au and AuPt), regardless of the presence of H_2O_2 against both *E. coli* and *S. aureus* (Fig. S19) indicating no antibacterial effect under physiological conditions (pH 7.4).

As this lack of antimicrobial effect could be due to either an

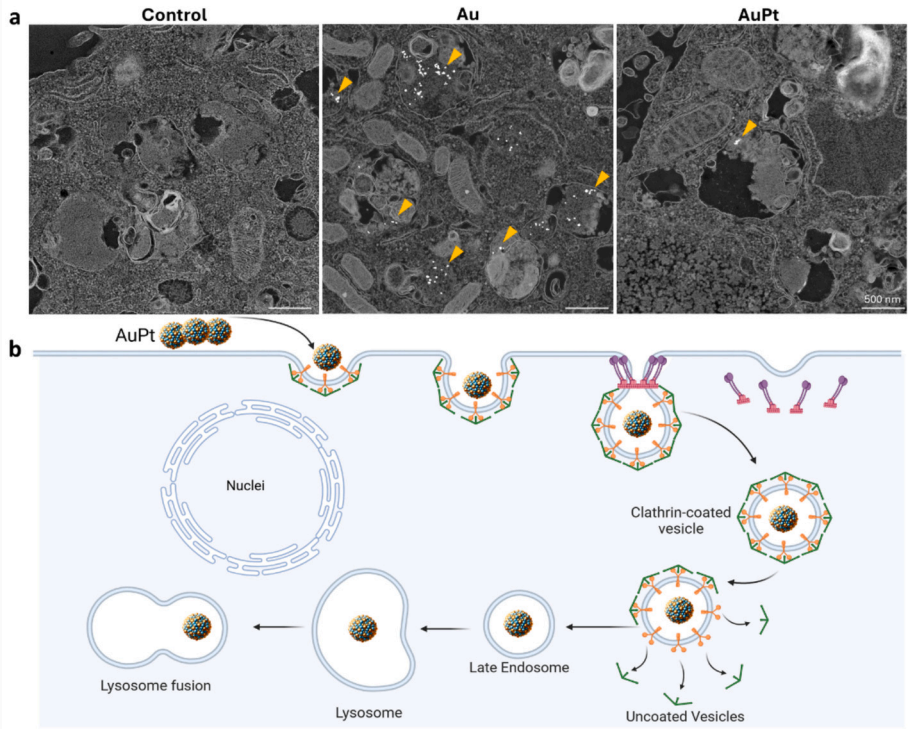

Fig. 6. Cellular internalization of nanozymes. a) Representative STEM images of 3 T3 fibroblast cells alone or incubated with Au or AuPt nanozymes. Nanozymes (white bright dots) are primarily found in multi-vesicular bodies or lysosome-like structures, as indicated by yellow arrowheads. d) suggested non-phagocytic nanozyme internalization pathways, clathrin-mediated endocytosis, and subsequent trafficking to the endosomal-lysosomal pathway.

inappropriate nanozyme concentration or an unsuitable substrate concentration, we extended our investigation by treating *E. coli* and *S. aureus* with varying AuPt nanozyme concentrations (0–100 μg/mL) in the presence of different H_2O_2 concentrations (0–8 mM). Interestingly, the results showed that AuPt nanozyme protected both *E. coli* (Fig. S20) and *S. aureus* (Fig. S21) from oxidative stress and even promoted their growth, particularly at high nanozyme concentrations (50 and 100 μg/mL). Indeed, while an 8 mM H_2O_2 concentration decreased *E. coli* (Fig. 7a) and *S. aureus* (Fig. 7b) survival rate to below 30%, AuPt treatment (50 and 100 μg/mL) significantly increased the survival rate to higher than 90%. This unexpected result is most likely due to the dominant CAT activity of AuPt in physiological conditions, which is aligned with the results on mammalian cells described in Fig. 4h.

Given the pH-dependent peroxidase (POD) activity of the nanozymes, we next explored their antibacterial efficacy in a slightly acidic environment (pH 5.5) against *E. coli* and *S. aureus* (Fig. 7c). The results demonstrated a significant reduction in colony numbers for both bacterial strains in the groups treated with AuPt nanozyme (25 μg/mL) and H_2O_2 (0.5 mM). In particular, the colony-forming units (CFUs) for *E. coli* were significantly lower in the AuPt + H_2O_2 condition (5×10^3 CFU/mL) compared to the Au + H_2O_2 (8×10^6) and the control + H_2O_2 group (9×10^6) (Fig. 7d). Similarly, AuPt exhibited a higher reduction in the colony number of *S. aureus* compared to Au and the control group, after H_2O_2 treatment (Fig. 7e).

Moreover, live/dead and DCFH-DA staining were performed to investigate the viability and intracellular ROS level of bacteria (Fig. 7f). The live/dead staining result revealed that AuPt-treated bacteria, with and without H_2O_2, exhibited lower cell viability and a higher amount of dead cells compared to the control and Au group, which showed only a few dead bacteria with no H_2O_2 treatment. Moreover, the DCFH-DA staining confirms the generation of hydroxyl radicals in bacteria in the presence of AuPt.

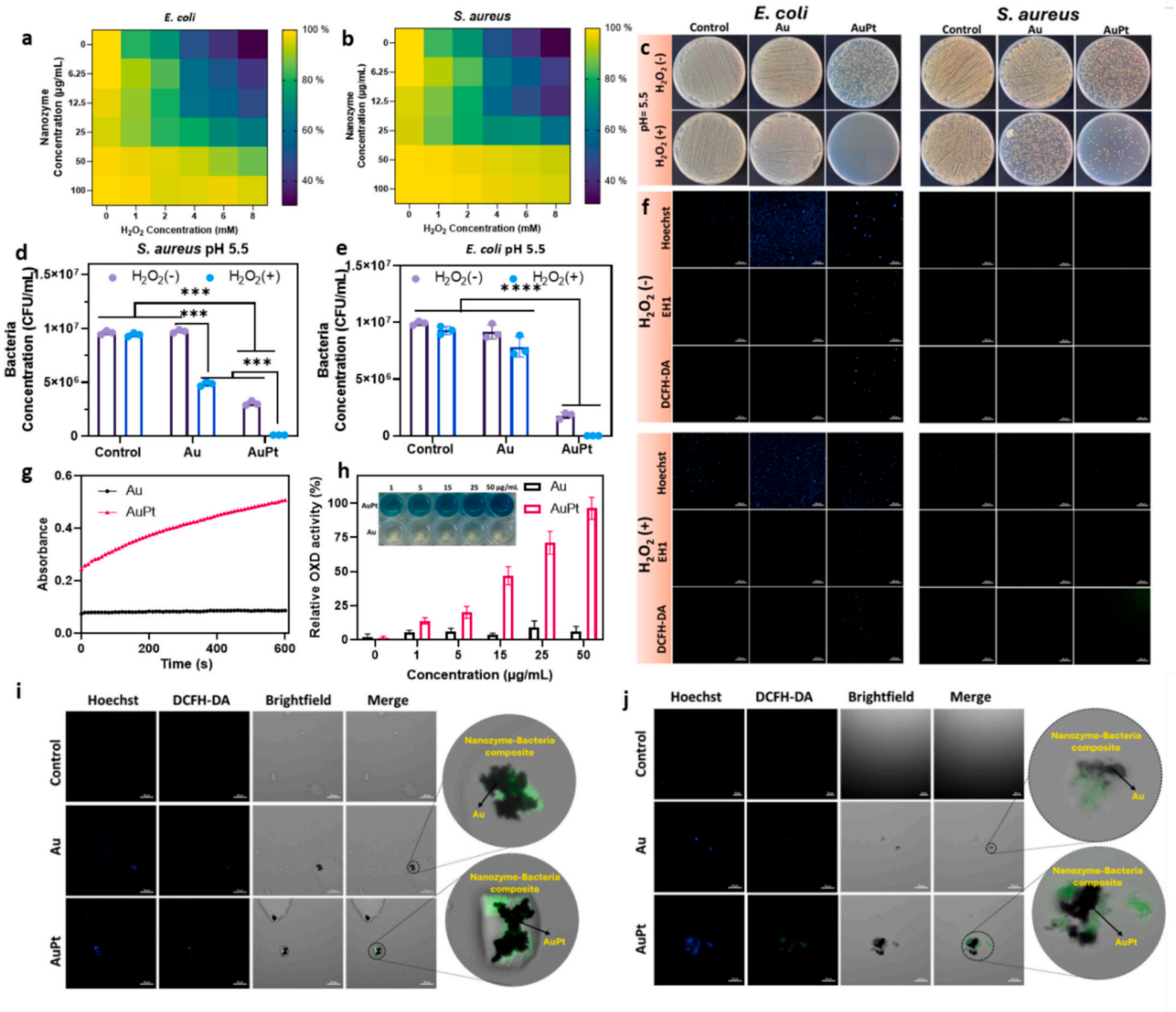

Fig. 7. In vitro antibacterial activity of nanozymes. Bacterial survival rate (%) of *E. coli* (a) and *S. aureus* (b), treated with different concentrations of AuPt (0–100 μg/mL) in the presence of H_2O_2 (0–8 mM). c) plate photographs for *E. coli* and *S. aureus* treated Au and AuPt, and control in the presence and absence of H_2O_2 at pH 5.5. Colony forming unit (CFU) countings of *E. coli* (d) and *S. aureus* (e) after treatment at pH 5.5. f) Fluorescent live/dead and DCFH-DA staining of *E. coli* and *S. aureus* treated with nanozymes in the presence and absence of H_2O_2 at pH 5.5. g) Oxidized-like (OXD) activity of Au, and AuPt is measured by the change in the absorbance of TMB at 625 nm versus time. h) Concentration-dependent relative OXD activity of Au, and AuPt. i) DCFH-DA fluorescent staining of *E. coli* treated with Au and AuPt in the presence of H_2O_2. j) DCFH-DA fluorescent staining of *S. aureus* treated with Au and AuPt in the presence of H_2O_2.

Interestingly, the AuPt nanozyme could inhibit the bacteria's growth compared to Au nanozyme even in the absence of H_2O_2, which likely could be due to its oxidase activity in an acidic environment, as well as its GOD-POD cascade reaction, which could effectively generate hydroxyl radical from the generated H_2O_2 from the glucose present in the bacteria medium. Hence, we next investigated the oxidase activity (OXD) of both Au and AuPt nanozyme using the TMB assay in the absence of H_2O_2 (Fig. 7g), and the results showed a significant increase in absorbance of TMB at 652 nm, indicating a higher OXD activity for AuPt. Moreover, the OXD activity of AuPt was concentration-dependent and the nanozyme at low concentration (below 0.5 μg/mL) did not show any significant activity (Fig. 7h). Hence, in an acidic environment, AuPt not only could effectively kill bacteria at a low H_2O_2 concentration (0.5 mM) but also could significantly inhibit bacterial growth due to its OXD activity [48,49]. A minor contribution from residual GOD activity coupled with POD may also play a role, but this requires further quantification.

Interestingly, in the presence of H_2O_2, Au, and AuPt nanozymes exhibited a tendency to form large aggregates when incubated with bacteria, as observed in brightfield microscopy (Fig. 7i for *E. coli* and Fig. 7j for *S. aureus*). Closer examination revealed that bacterial cells were frequently localized around these nanozyme aggregates and formed a bacteria-nanozyme composite, particularly with *S. aureus*, likely due to the negative surface charge of the nanozyme, which led to electrostatic interactions [50]. Interestingly, DCFH-DA fluorescence was predominantly localized within these nanozyme-bacteria composites, whereas planktonic (free-floating) bacteria exhibited minimal fluorescence, suggesting that the initiation of ROS-mediated antibacterial activity in the AuPt + H_2O_2 system primarily occurs at the interface between the nanozymes and the bacterial cells. The co-localization of ROS production and nanozyme aggregates indicates that the antibacterial mechanism is highly localized, enhancing the effectiveness of ROS in eliminating bacteria at the interaction sites between nanozyme and bacteria [51]. Since chronic diabetic wounds are mostly alkaline, the antibacterial effect may not fully translate. Future strategies (e.g., pH-modulating agents or photoacids) could enhance antibacterial efficacy in such environments.

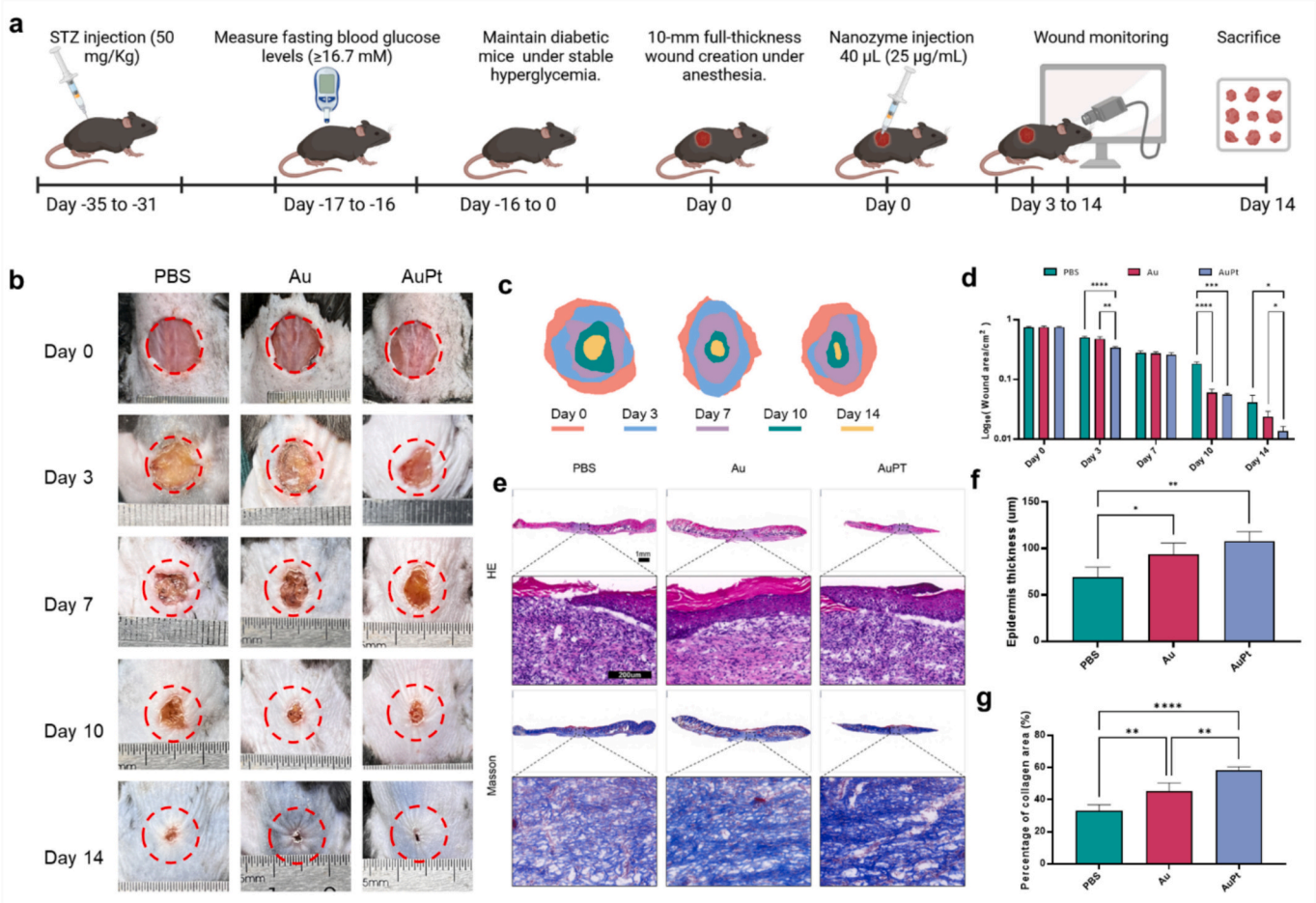

Fig. 8. Evaluation of wound healing progression and histological evaluation of wound healing. a) Schematic procedure of the infected diabetic wound model and treatment. b) Representative photographs of wound sites in mice treated with PBS (control), Au, and AuPt nanozyme on days 0, 3, 7, 10, and 14. The red dashed circles indicate the initial wound size with a diameter of 1 cm at day 0. c) Schematic representation of wound area reduction over time for the different treatment groups. The color-coded layers represent the wound area on days 0, 3, 7, 10, and 14. d) Quantitative analysis of wound areas measured on days 0, 3, 7, 10, and 14 using ImageJ software. Data are presented as the log-transformed wound area (cm^2) for each group. Statistical significance was determined using one-way ANOVA followed by post hoc tests. $^*p < 0.05$, $^{**}p < 0.01$, $^{***}p < 0.001$, $^{****}p < 0.0001$. Error bars represent mean ± standard deviation (SD), with $n = 5$ per group. e) Representative wound sections stained with H&E (top row) and Masson's trichrome treated with PBS (control), Au nanozyme, and AuPt nanozyme at day 14 post-injury. Upper panels display the overall wound sections, and lower panels show magnified views of the corresponding regions (scale bars: 1 mm for the overall sections; 200 μm for magnified views). f) Quantification of epidermal thickness (μm) in wounds from different treatment groups. g) Quantification of collagen deposition as the percentage of collagen-positive area in Masson's trichrome-stained sections. Data are presented as mean ± standard deviation (SD). Statistical analysis was performed using one-way ANOVA followed by post hoc tests and multiple comparison tests. *p < 0.05, **p < 0.01, ****p < 0.0001.

2.5. In vivo wound healing

To evaluate the therapeutic efficacy of nanozymes in diabetic wound healing, an in vivo wound healing study was performed on a diabetic mouse model. The timeline of the experimental protocol is outlined in Fig. 8a. Briefly, diabetes was induced in male C57BL/6 mice through repeated intraperitoneal administrations of streptozotocin (STZ, 50 mg/kg) over five days, and diabetic status was confirmed by fasting blood glucose levels ≥16.7 mM. After maintaining stable hyperglycemia for four weeks, full-thickness 10-mm diameter wounds were created under anesthesia, followed by the topical administration of either PBS (control), Au nanozyme, or AuPt nanozyme (40 μL, 25 μg/mL). In this proof-of-concept study, a single dose (25 μg/mL) was chosen based on in vitro biocompatibility and catalytic activity. Future dose-ranging studies will be required to identify minimal effective and optimal therapeutic concentrations. The wound healing progression was monitored over 14 days [52].

Wound area measurements revealed that treatment with AuPt nanozyme significantly enhanced wound closure compared to PBS and Au nanozyme groups. Visual documentation of the wound sites on days 0, 3, 7, 10, and 14 post-injury (Fig. 8b,c), highlights a pronounced reduction in wound area for the AuPt-treated group. Furthermore, quantitative analysis (Fig. 8d) revealed that the mean log-transformed wound area for the AuPt group at day 14 was 0.014 ± 0.003, which was significantly smaller than both the PBS group (0.042 ± 0.011, $p < 0.0001$) and the Au group (0.024 ± 0.006, $p < 0.01$).

Histological analyses were conducted on day 14 post-injury to evaluate epidermal regeneration and extracellular matrix (ECM) remodeling in the wound tissues. Hematoxylin and eosin (H&E) staining (Fig. 8e) revealed differences in epidermal thickness across the treatment groups. Wounds treated with AuPt nanozyme displayed a well-formed, stratified epidermal layer, in contrast to the PBS group, which exhibited incomplete re-epithelialization with thin and disorganized epidermal tissue. Quantitative measurements of epidermal thickness (Fig. 8f) confirmed that the AuPt-treated group achieved significantly thicker epidermal layers (107.36 ± 9.2 μm, $p < 0.05$) compared to the Au group (93.48 ± 11.0 μm) and PBS group (69.35 ± 10.1 μm) indicating that AuPt nanozyme accelerates epidermal regeneration and promotes organized skin structure formation.

Masson's trichrome staining was conducted to evaluate collagen deposition, as an indicator of ECM remodeling (Fig. 8e). Wounds treated with AuPt exhibited a dense and well-organized collagen network, whereas the PBS group demonstrated sparse collagen deposition with disrupted structure. Quantitative analysis (Fig. 8g) exhibited that collagen-positive areas were significantly higher in the AuPt-treated group (58.78 ± 2.06%, $p < 0.01$) compared to the Au group (45.80 ± 5.03%) and PBS group (33.62 ± 3.72%). The results confirm the tissue regeneration capacity of AuPt nanozymes through enhanced collagen remodeling; however, potential cumulative effects and long-term retention of noble metals in vivo should be considered in future investigations.

To assess the inflammatory response in wound tissues, the ROS levels were measured using dihydroethidium (DHE) staining of cryosectioned wound tissues, along with TNF-α and IL-1β expression at day 14 post-injury. The fluorescence images of ROS detection (Fig. 9a) demonstrated that the PBS group exhibited intense ROS fluorescence signals, indicating elevated oxidative stress in untreated wounds. In contrast, Au-treated wounds displayed moderate ROS levels, while AuPt-treated wounds showed negligible ROS fluorescence. Quantitative analysis (Fig. 9b) revealed that the percentage of ROS-positive areas in the PBS group was significantly higher (28.3 ± 4.2%) compared to the Au (10.58 ± 2.1%) and AuPt groups (1.9 ± 0.8%, $p < 0.0001$).

The expression levels of pro-inflammatory cytokines TNF-α (Fig. 9c) and IL-1β (Fig. 9d) were also quantified to further assess inflammation.

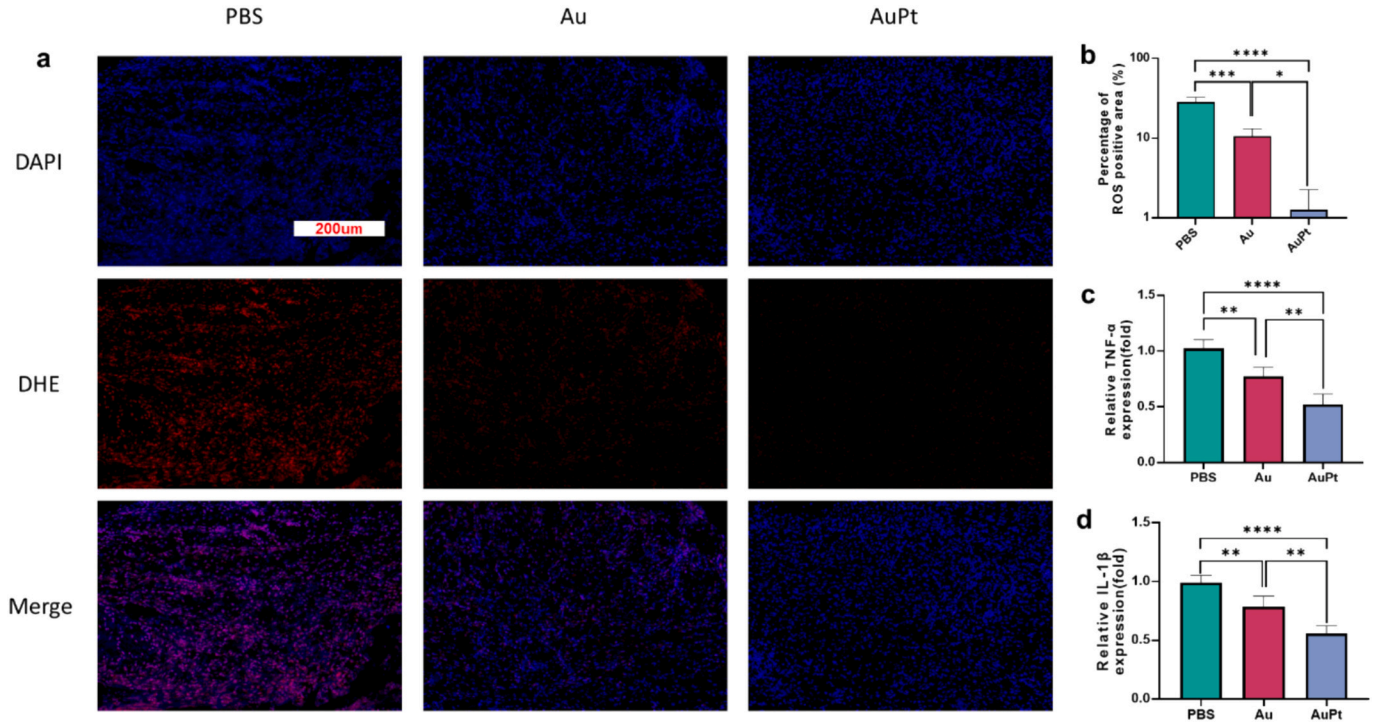

Fig. 9. Evaluation of ROS levels and inflammation in wound tissues treated with different nanozymes. a) Representative fluorescence images of wound sections stained for ROS (red, DHE staining) and nuclei (blue, DAPI staining) from mice treated with PBS (control), Au nanozyme, and AuPt nanozyme at day 14 post-injury. Merged images show the overlay of DHE and DAPI signals. Scale bar = 200 μm. b) Quantification of the percentage of ROS-positive area in wound sections for each treatment group. Quantification of relative TNF-α expression levels (c) and IL-1β expression levels (d) in wound tissues treated with PBS (control), Au nanozyme, and AuPt nanozyme at day 14 post-injury. Data are presented as mean ± standard deviation (SD). Statistical analysis was performed using one-way ANOVA followed by post hoc tests. *$p < 0.05$, **$p < 0.01$, ***$p < 0.001$, ****$p < 0.0001$.

Both TNF-α and IL-1β levels were significantly lower in the AuPt-treated group compared to PBS and Au-treated groups. Specifically, TNF-α expression was reduced by approximately 50% in the AuPt group relative to the PBS group ($p < 0.001$), while IL-1β levels were reduced by 60% ($p < 0.01$). These reductions indicate a dampened inflammatory response in wounds treated with AuPt nanozymes, further supporting their role in creating a microenvironment conducive to tissue repair. Previous studies have demonstrated that platinum nanozymes (PtNZs) can actively modulate inflammatory responses through redox-mediated pathways. In particular, PtNZs exhibiting SOD- and CAT-like activities effectively reduce intracellular ROS overproduction and downregulate NF-κB-dependent cytokine release in LPS-stimulated macrophages [53,54]. These anti-inflammatory effects have been attributed to the ability of Pt-based nanozymes to quench ROS within endolysosomal compartments and restore redox homeostasis in immune cells, thereby reducing pro-inflammatory signalling and promoting tissue repair [55]. This evidence supports the potential role of AuPt nanozymes in metallo-immunomodulation via catalytic redox regulation.

3. Conclusion

In this study, we successfully developed a bimetallic AuPt nanozyme using tannic acid with multi-enzyme mimetic activities as a potential therapeutic solution to address the multifaceted challenges of diabetic wound healing. By combining the glucose oxidase-like activity of Au with the peroxidase, catalase, and superoxide dismutase-like activities of Pt, AuPt nanozyme could effectively balance oxidative stress, and present antimicrobial properties. Moreover, in a diabetic wound model, AuPt nanozyme exhibited superior epidermal regeneration and collagen deposition, mitigated inflammation, evidenced by decreased TNF-α and IL-1β expression. This work highlights the potential of polyphenol-assisted AuPt nanozymes as a novel, effective therapy for diabetic wounds. Although short-term in vitro and in vivo studies confirmed biocompatibility, the long-term biodistribution, clearance, and accumulation of Au and Pt remain unknown. These factors will need rigorous evaluation before considering translation toward chronic wound therapy. Future studies integrating direct oxygen measurements, immune profiling, and long-term biodistribution will be essential to fully delineate the dominant in vivo mechanisms.

4. Materials and methods

4.1. Chemicals and materials

chloroplatinic acid ($H_2PtCl_6{\cdot}6H_2O$), tetrachloroauric(III) acid trihydrate 99% ($HAuCl_4{\cdot}3H_2O$), tannic acid, Hydrogen peroxide (H_2O_2, 30%), Dimethyl sulfoxide (DMSO), 3,3′,5,5′-Tetramethylbenzidine (TMB), Pyrogallol, dihydroethidium (DHE), tris(4,7-diphenyl-1,10-phenanthroline) ruthenium (II) dichloride complex, 2′,7′-Dichlorodihydrofluorescein diacetate, sodium hydroxide (NaOH), horseradish peroxidase (HRP, lyophilized, powder, ~150 U/mg), acetic acid glacial, sodium acetate, hydrochloric acid (HCl), phosphate-buffered saline (PBS), sodium chloride (NaCl), Tris-HCl buffer, streptozotocin (STZ), Hoechst 33342, ethdium homodimer-1 (EthD-1), menadione, paraformaldehyde (PAF), glutaraldehyde, sodium cacodylate trihydrate, osmium tetroxide, ferrocyanide, uranyl acetate, and epoxy resin (AGAR100) were purchased from Sigma-Aldrich. Cyanine5.5 NHS ester was purchased from Lumiprobe GmbH (Hannover, Germany). Alexa Fluor 488 – Phalloidin (ab176753) was purchased from Abcam, Belgium.

4.2. Instrumentation

Transmission Electron Microscopy, including HR-TEM, SAED, and STEM, was acquired using a ThermoFisher Talos 200C (Thermo Fisher Scientific, Waltham, MA, USA) equipped with a field-emission gun operated at 200 kV. Powder X-ray diffraction (XRD) data were acquired with an ecoD8 advance system, scanning in the range of $5° < 2\Theta < 90°$ at a rate of 1.2° per minute. Energy Dispersive X-ray (EDX) spectra were obtained using a Thermo Fisher Talos F200X instrument. X-ray photoelectron spectroscopy (XPS) spectra were recorded using a FISONS S-PROBE with an Al-Kα source (1486 eV), developed by Fisons Instruments Surface Science (Sanofi, Paris, France). The size and zeta potential of the nanozymes were measured with a Malvern Zetasizer Nano ZSE. UV–Vis absorption spectra and kinetic absorbance measurements were performed using a Tecan Spark multimode microplate reader (Tecan Trading AG, Männedorf, Switzerland). Confocal laser scanning microscopy (CLSM) was conducted using a ZEISS LSM 900 microscope for cellular uptake and colocalization studies. Catalase activity was analyzed using a PreSens contactless oxygen meter sensor. High-angle annular dark-field scanning TEM (HAADF-STEM) images were obtained with a ThermoFisher Talos 200C. Fluorescence microscopy for antibacterial studies was performed using a Zeiss Axio Observer microscope.

4.3. Synthesis of core-shell AuPt nanozyme

Core-shell AuPt nanozyme was synthesized via one-spot reaction using tannic acid as a reducing agent. Briefly, $HAuCl_4{\cdot}3H_2O$ and $H_2PtCl_6{\cdot}6H_2O$ were dissolved in 40 mL of deionized water at a final concentration of 1 mM each. Then, 10 mL of tannic acid (TA) solution (4 mg/mL) was dropwise added to the solution, and the color immediately changed to dark purple. The pH was adjusted to 7.4 using 1 M NaOH and monitored during the reaction for 4 h at 60 °C. The AuPt nanozymes were isolated via centrifuging at 12,000 RPM and washing three times with ultrapure water to remove residual reagents. The Au nanozyme was synthesized using the same method without the addition of $H_2PtCl_6{\cdot}6H_2O$.

4.4. Multienzyme-like activity

4.4.1. The peroxidase (POD) activity

The POD activity of the nanozymes was investigated using TMB assay according to a method reported previously [56]. The ability of nanozyme to oxidize TMB (oxTMB) was determined at 652 nm using a UV–vis spectrophotometer. Briefly, the Au and AuPt with different concentrations (0.05 to 0.25 μg/mL) were mixed with TMB (2 mM) solution and H_2O_2 (1 M) in 1 mL of acetic acid-sodium acetate Buffer (NaAc-Hac) (pH 4.0). The absorbance was recorded as a function of reaction time. The nanozyme's specific activity (SA) was determined according to the following equation:

$$SA = (V/(\varepsilon \times l) \times (\Delta A/\Delta t))/m \quad (1)$$

Where V represents the total volume of the reaction mixture (μL). The ε denotes the molar absorption coefficient for the colorimetric substrate, 39000 M^{-1} cm^{-1} at 652 nm, for TMB. The 'l' refers to the path length that the light travels through within the cuvette, measured in centimeters (cm). 'A' is the absorbance value, adjusted by subtracting the blank's absorbance. ΔA/Δt is the initial rate of change in absorbance at 652 nm (min^{-1}). Lastly, 'm' indicates the weight of the nanozyme used in each assay, measured in milligrams (mg).

The steady-state POD kinetics of nanozymes were assessed at different TMB concentrations (0–1 mM) and constant concentration H_2O_2 (1 M). For the kinetic assay, 0.25 μg/mL of AuPt nanozyme and 2.5 μg/mL of Au nanozyme were used, respectively. Kinetic parameters were measured by fitting experimental data to Michaelis-Menten equation:

$$V = \frac{V_{max}[S]}{K_m + [S]} \quad (2)$$

V_{max} represents the maximal reaction velocity, K_m represents the

Michaelis-Menten constant.

4.4.2. The catalase (CAT) activity

Nanozymes' CAT-like activity was examined by measuring the generated oxygen using a contactless oxygen meter sensor (PreSens, Regensburg, Germany) [57]. The oxygen generation (mg/L) induced by nanozyme at different concentrations (0–5 μg/mL), in the presence of H_2O_2 (60 mM) was recorded for 10 min. Moreover, the kinetic assay of the catalytic decomposition of H_2O_2 was performed at a different concentration of H_2O_2 (0–100 mM) and a constant concentration of nanozyme (3 μg/mL). The experimental data were analyzed using Michaelis-Menten equation to determine the V_{max} and K_m.

Additionally, to determine the H_2O_2 scavenging of the nanozyme as a CAT mimic, the diminishing concentration of H_2O_2 was observed over time at 240 nm by using a UV–Vis spectrophotometer [23]. The reaction mixture consisted of 10 mM H_2O_2 and nanozymes at a concentration of 25 μg/mL, in a 500 μL volume of PBS (25 mM, pH 7.4). The decrease in the absorbance peak at 240 nm of the solution was continuously tracked by using UV–vis spectroscopy for 10 min.

The specific CAT activity (U/mg) of nanozymes was investigated using the generated oxygen as the byproduct of the catalytic decomposition of hydrogen peroxide, measured by a contactless oxygen meter sensor (PreSens, Regensburg, Germany). A unit of CAT activity corresponds to the amount of enzyme required to decompose 1 μmole of hydrogen peroxide per minute. Hence, the amount of oxygen generated (mg/L) was converted to μmole of oxygen, and the specific activity was measured using the following equation:

$$\text{Specific CAT activity (U/mg)} = \frac{2 \times (\mu\text{mole of oxygen per minute})}{\text{Mass of nanozyme (mg)}} \quad (4)$$

The factor of 2 in the equation accounts for the stoichiometry of the reaction, where each molecule of hydrogen peroxide (H_2O_2) yields half a molecule of oxygen (O_2).

4.4.3. The superoxide dismutase (SOD) activity

The SOD activity was evaluated by evaluating the nanozyme's capability to inhibit the pyrogallol self-oxidation rate [58]. The pyrogallol self-oxidation in alkaline conditions in the presence of EDTA as a chelating agent, leads to the generation of purpurogallin, proportional to $O_2^{\bullet -}$ with maximum absorbance at 325 nm. Briefly, the auto-oxidation was measured in 1 mL of Tris-HCl buffer (0.05 mM, pH 8.4) including pyrogallol (75 μM) and EDTA (2 mM) via monitoring absorbance at 325 nm over time for 10 min. Different concentrations of nanozyme (0–50 μg/mL) were used to evaluate the inhibition rate of the pyrogallol self-oxidation rate and the IC_{50} using the following equation:

$$\textbf{Oxidation rate of pyrogallol}\ (\%) \frac{\mathbf{R}_{\text{self-oxidation}} - \mathbf{R}_{\text{nanozyme-oxidation}}}{\mathbf{R}_{\text{self-oxidation}}} \times \mathbf{100\%} \quad (5)$$

where $R_{self\text{-}oxidation}$ represents the rate of pyrogallol autoxidation in the absence of nanozymes, and $R_{nanozyme\text{-}oxidation}$ denotes the rate of pyrogallol oxidation following the addition of either Au or AuPt nanozymes.

Moreover, the kinetic assay was carried out at different concentrations of pyrogallol (0–20 mM) at a constant concentration of nanozyme (50 μg/mL). The experimental data were fitted to the Michaelis-Menten equation to calculate the V_{max} and K_m.

4.4.4. The Glucose oxidase (GOD) activity

The GOD activity of the nanozyme was evaluated by the ability of the nanozyme to catalyze the oxidation of glucose to H_2O_2 using the TMB assay [59]. Briefly, the Au and AuPt with different concentrations (5 μg/mL) were mixed with a glucose solution (100 mM) in 1 mL of NaAc-HAc buffer (pH 4.0) containing TMB (2 mM) and HRP (0.01 mg/mL). The oxidation of TMB was determined by a change in the absorption at 652 nm. Moreover, the kinetic assay was performed at different concentrations of Glucose (0–100 mM), at the constant concentration of nanozyme (5 μg/mL), TMB (2 mM), and HRP (0.01 mg/mL). The experimental data were fitted to the Michaelis-Menten equation to determine the V_{max} and K_m.

4.4.5. DFT calculations

The AuPt core-shell nanozyme was simulated using Density Functional Theory (DFT) with the Quantum ESPRESSO package [60,61]. The Perdew–Burke–Ernzerhof (PBE) functional was used to describe the exchange-correlation effects. The nanozyme was modeled using a slab (with a 3 × 3 surface supercell), composed of a 5-layer Au core and a 2-layer Pt shell, plus 15 Å of vacuum. The lattice parameters and the atomic positions were fully relaxed. This slab model was selected to reflect the experimentally observed core-shell structure, as supported by TEM/EDX mapping (Fig. 1a–b), and is further validated by the simulated XRD pattern (Fig.. S17), which reproduces the (111) reflections of both Au and Pt.

To sample the Brillouin zone, a 3 × 3 × 1 Monkhorst-Pack grid was used for the geometry optimization, while a denser 6 × 6 × 1 grid was adopted for the SCF calculations to ensure precise energy values. Convergence thresholds for the calculations were set to 1.0×10^{-8} Ry for SCF energy convergence. Adsorption energies for H_2O_2 and O_2^- on the slab were calculated using the total energies obtained from the SCF calculations as $E_{ads} = E_{slab+adsorbate} - E_{slab} - E_{adsorbate}$, providing insights into the binding strength of the reactive species on the surface.

Additionally, a Bader charge analysis was conducted to study the electron redistribution upon adsorption, offering a deeper understanding of the charge transfer processes during catalytic activity.

4.5. Cytotoxicity evaluation

The impact of Au and AuPt nanozymes on the fibroblast 3 T3-L1 cells' viability was investigated through the CellTiter 96® AQ_{ueous} One Solution Cell Proliferation Assay (MTS). 3 T3-L1 fibroblasts (passage 9), kindly provided by Dr. I. Pirson [62], were cultured in high-glucose DMEM supplemented with 10% fetal calf serum (FCS), 200 U/mL penicillin, and 200 U/mL streptomycin, maintained in a humidified incubator with 5% CO_2. Cells were seeded and allowed to adhere for 24 h, after which the medium was replaced with DMEM containing varying levels of nanozymes (0–100 μg/mL). Following 24 or 48 h of incubation, the DMEM was removed, and a combination of 180 μL DPBS and 20 μL MTS solution (5 mg/mL) was added to each well, followed by an additional 4 h of incubation, and then the absorbance was monitored at 490 nm using a microplate reader to determine the cell viability.

Moreover, the biocompatibility of nanozyme was investigated using Live/Dead assay, followed by co-staining with Hoechst 33342 and Ethidium Homodimer-1 (EthD-1). Fibroblast 3 T3 cells were cultured in 8 well-plates, and incubated for 24 h, followed by 48 h of incubation with nanozyme at a concentration of 25 μg/mL. Subsequently, the DMEM was aspirated, and the cells were incubated with Hoechst 33342 (10 μM) and EthD-1 (10 μM) for staining for 30 min, followed by washing with DPBS. Cells were visualized using a confocal laser scanning microscope (Zeiss LSM900, Germany).

4.6. Cell migration assay

Cell migration assay was performed according to a previous report [63]. 3 T3-L1 cells (230,000 cells per well) were seeded in a medium containing 10% FCS using culture-insert 2 wells (Ibidi, Gräfelfing, Germany), which created a defined cell-free gap of 500 μm ± 50 μm within a well area of 0.22 cm^2. After 24 h of incubation in a medium containing 1% FCS, the inserts were removed, and the cells were exposed to Au and AuPt treatments at a concentration of 25 μg/mL. Images were captured at 0-, 4-, and 24-h post-insert removal, and the ImageJ software (Version 1.8.0, NIH, USA) was used to analyze the images.

4.7. Intracellular ROS and O_2 level

The capability of the nanozymes to mimic antioxidant activity and scavenge intracellular ROS was examined using specific fluorescent probes [23]. 3 T3 cells were seeded in an Ibidi μ-Slide 8-well and cultured for 24 h. Then the cells were treated with Au and AuPt nanozyme (25 μg/mL) for 24 h. The excess nanozymes were removed by washing with DPBS three times, followed by H_2O_2 (100 μM) treatment for 4 h to induce oxidative stress. Then the cells were stained using 2′,7′-dichlorofluorescein diacetate (DCFH-DA) fluorescent probe (10 μM) for 45 min to determine the intracellular ROS level. To detect the intracellular O_2, the cells were treated as mentioned above and stained using tris (4,7-diphenyl-1,10-phenanthroline) ruthenium (II) dichloride complex ($[Ru(dpp)_3]Cl_2$, RDPP) for 45 min at 37 °C. The cells were analyzed using a confocal laser scanning microscope. To determine the intracellular SOD activity of the nanozyme, the cells were seeded and incubated with the nanozyme. The cells were incubated with Menadione (50 μM) as a ROS inducer to induce intracellular production of ROS (mostly superoxide) [64]. Then, the cells were stained using dihydroethidium (DHE) fluorescence probe (37 °C for 30 min) to determine the Intracellular $O_2^{\bullet-}$ level. ROS and SOD activity assays were performed under normoxic conditions (~21% O_2).

4.8. Oxidative damage protection

The protective role of Au and AuPt nanozymes against induced oxidative stress in fibroblast 3 T3 cells was quantified by pre-treating the cells with the nanozymes (25 μg/mL), followed by exposure to H_2O_2 with different concentrations (0–1 mM) for 8 h. The MTS assay was carried out to assess cell viability.

4.9. Cellular uptake and distribution analysis

The cellular uptake and distribution of Cy5.5-conjugated nanozymes within fibroblast 3 T3 cells were investigated using LysoTracker™ Green DND-26. The Cy5.5 labeling was carried out according to the previous report with some modifications [65]. First, Au and AuPt nanozymes (1.5 mg/mL, 0.5 mL) were functionalized with L-cysteine (10 mM, 50 μL) in 5 mL PBS to introduce amine groups via thiol attachment to the metal surface. The mixture was incubated for 1 h at room temperature with gentle mixing, then centrifuged at 10,000 rpm for 15 min, washed with PBS, and resuspended. Then, 50 μL of Cy5.5-NHS ester (1 mg/mL in DMSO) was added to the functionalized nanozymes and incubated for 1 h at room temperature with stirring. The labeled nanozymes were purified by centrifugation (10,000 rpm, 15 min) and washed three times with PBS.

Fibroblast 3 T3 cells were cultured in 8 well-plate, and incubated for 24 h to adhere, followed by 24 h of incubation with Cy5.5-conjugated nanozymes (25 μg/mL). The cells were washed three times with DPBS to remove the excess nanozymes and then incubated with 100 μL of DPBS containing 50 nM LysoTracker Green and Hoechst 33342 (10 μM) for 30 min and the cells were observed using a confocal laser scanning microscope (ZEISS LSM 900) with laser excitation at 405 nm for Hoechst 33342, 488 nm for LysoTracker Green, and 633 nm for Cy5.5.

For cytoskeleton staining, the cells were treated with nanozymes (25 μg/mL) for 24 h. The cells were washed with DPBS and fixed with 4% paraformaldehyde (PAF) for 20 min at room temperature. Subsequently, the cells were stained with Hoechst 33342 (10 μg/mL) and 2 μM Alexa Fluor 488 Phalloidin (excitation at 488 nm) in DPBS containing 1% BSA at room temperature for 90 min [66]. The cells were examined using a confocal laser scanning microscope (ZEISS LSM 900, Zeiss, Germany).

For scanning Transmission electron microscopy, 3 T3 cells were seeded at 65000 cells/cm^2 in a 6-well plate to obtain at least a million cells at the end of the experiment. The day after seeding, Au and AuPt at 25 μg/mL were added to the culture for 24 h. At the end of the culture, cells were collected and fixed with 2.5% glutaraldehyde (EMS) diluted in 0.1 M sodium cacodylate trihydrate buffer (Merck Group, Germany). Pellets were then washed in cacodylate buffer, post-fixed in osmium 1% and ferrocyanide 1.5% for 1 h at RT, washed, incubated in an additional bath of osmium 1% for 1 h, washed in water, and colored in a uranyl acetate 1% solution for 2 h at RT. After washing, samples were progressively dehydrated using graded ethanol solutions (35% to 100%, 15 min each). Ethanol was replaced by propylene oxide 100%, and then the epoxy resin (AGAR100, Agar Scientific) was progressively infiltrated into the tissue. After acclimatization to the resin, samples were put in the oven at 60 °C for 72 h. Samples were then sectioned using an UC6 ultramicrotome (Leica) and ultra-thin sections (50 to 70 μm) were recovered on Cu grids (100 mesh, formvar/carbon-coated). Images were acquired on a ThermoFisher Talos 200C (Thermo Fisher Scientific, Waltham, MA, USA) equipped with a field-emission gun operated at 200 kV and Velox software.

4.10. In vitro antibacterial activity

To evaluate the antibacterial activity of the nanozyme, *Escherichia coli* ATCC 27195 (*E. coli*) and *Staphylococcus aureus* ATCC 25923 (*S. aureus*) were selected as representative Gram-negative and Gram-positive bacterial strains, respectively. Bacterial suspensions (10^6 CFU/mL) were treated with Au and AuPt nanozymes at a concentration of 25 μg/mL, in the presence and absence of H_2O_2 (0.5 mM). The treatment was performed in both neutral (pH 7.4) and slightly acidic (pH 5.5) conditions to assess the pH-dependent efficacy of the nanozymes. Following a 24-h incubation at 37 °C, the bacterial suspensions were serially diluted and spread onto LB agar plates for analysis [67]. The plates were incubated overnight at 37 °C, and the number of colonies was counted to determine the CFU. Moreover, to investigate the effect of the POD activity of the nanozyme on bacteria growth inhibition, different concentrations of AuPt with high POD activity were used in the presence of different concentrations of H_2O_2 (0 to 8 mM).

The bacteria's viability was assessed using live/dead staining with Hoechst 33342 and Ethidium Homodimer-1 (EthD-1). Bacterial suspensions treated with nanozymes and H_2O_2 were centrifuged, and the pellets were resuspended in PBS. Hoechst (10 μg/mL) and EthD-1 (2 μM) were added to the bacteria and incubated in the dark at room temperature for 20 min, followed by washing with PBS. Fluorescence microscopy (ZEISS Axio Observer microscope) was performed to visualize bacteria. Moreover, the ROS level in bacteria was measured using the fluorescent probe 2′,7′-dichlorodihydrofluorescein diacetate (DCFH-DA).

4.11. In vivo wound healing

All animal experiments were approved by the Animal Care Committee of Tongji Medical College, Huazhong University of Science and Technology (Approval Number 4831). A diabetic wound model was established using male C57BL/6 mice (6 weeks old, 15–25 g). To induce diabetes, streptozotocin (STZ, 50 mg/kg body weight; Biosharp, China) was injected intraperitoneally once daily for a period of five days. To enhance STZ absorption and diabetes induction efficiency, mice were fasted for 6 h prior to each injection. Fasting blood glucose levels were measured two weeks after the last injection by drawing blood from the tail vein and using a glucometer. Mice with fasting blood glucose levels ≥16.7 mM in two consecutive readings were classified as diabetic. Diabetic mice were maintained on a standard diet and monitored for four additional weeks to ensure stable hyperglycemic conditions. Mice were anaesthetized with an intraperitoneal injection of 1% sodium pentobarbital (50 mg/kg; Sigma, USA), followed by shaving and sterilization of the dorsal fur. A full-thickness circular skin wound (10-mm diameter) was created on the dorsum using a sterile biopsy punch. Following wound creation, mice were randomly assigned to three treatment groups ($n = 5$ per group); PBS (control), 40 μL of 25 μg/mL Au, and AuPt nanozyme (25 μg/mL) applied topically to the wound

surface using a micropipette. The 25 μg/mL dose was chosen as it showed strong intracellular catalytic activity while maintaining >80% fibroblast viability in vitro. Wound healing was monitored through photographs taken on days 0, 3, 7, 10, and 14 using a high-resolution digital camera. Wound areas were measured using ImageJ software to calculate the rate of closure over time. On day 14, wound tissues were collected, embedded in OCT compound, and cryosectioned into 8-μm-thick slices. To assess inflammation, granulation tissue formation, and re-epithelialization, sections underwent hematoxylin and eosin (H&E) staining. Additionally, collagen deposition and extracellular matrix remodeling were analyzed using Masson's trichrome staining. To evaluate ROS levels, cryosectioned wound tissues (8 μm) were stained with dihydroethidium (DHE). Fluorescence microscopy was used to capture images of ROS signals, and quantitative analysis was conducted using ImageJ software.

4.12. Statistical analysis

All statistical analyses were carried out using GraphPad Prism 9.0 (GraphPad Software, USA). Data are expressed as mean ± standard deviation (SD). For in vitro assays and enzyme kinetics, comparisons among groups were performed using one-way ANOVA followed by Tukey's multiple comparisons test. For wound closure rates and other time-dependent datasets, two-way ANOVA with repeated measures was applied, followed by Bonferroni post hoc test. A minimum of three independent experiments were conducted for in vitro studies, and animal studies included n = [5] mice per group. Differences were considered statistically significant at $p < 0.05$.

CRediT authorship contribution statement

Hafez Jafari: Writing – original draft, Visualization, Validation, Software, Methodology, Investigation, Funding acquisition, Formal analysis, Data curation, Conceptualization. **Lizhao Yan:** Methodology, Investigation, Formal analysis. **Elham Dehghanpisheh:** Software, Methodology, Formal analysis. **Pejman Ghaffari-bohlouli:** Methodology. **Erika Hendrickx:** Methodology, Investigation, Formal analysis. **Louise Conrard:** Writing – review & editing, Methodology. **Gian-Marco Rignanese:** Writing – review & editing. **Lei Nie:** Writing – review & editing, Methodology. **Armin Shavandi:** Writing – review & editing, Validation, Supervision, Project administration. **Peter Dubruel:** Writing – review & editing, Supervision, Resources, Project administration, Methodology.

Declaration of competing interest

The authors declare that they have no known competing financial interests or personal relationships that could have appeared to influence the work reported in this paper.

Acknowledgment

H.J. acknowledges financial support from the Special Research Fund (BOF) of Ghent University (BOF23/PDO/042). The authors acknowledge the Center for Microscopy and Molecular Imaging (CMMI, ULB and UMONS) for access to TEM facilities; CMMI is supported by the Walloon Region and European funding (FEDER). The authors further acknowledge the Walloon Region for financing, in whole or in part, the equipment used in this study through the Technology Platforms of Excellence, *Alternative to animal experimentation,* and *Biogreen*. H.J. also acknowledges Université libre de Bruxelles (ULB) for support through a scientific collaborator position. A.S. and H.J. also acknowledge Innoviris Brussels for financial support. A.S. acknowledges support from the FNRS under the CDR grant J.0188.24.

Appendix A. Supplementary data

Supplementary data to this article can be found online at https://doi.org/10.1016/j.cej.2026.173306.

Data availability

Data will be made available on request.

References

[1] H. Wu, F. Li, W. Shao, J. Gao, D. Ling, Promoting angiogenesis in oxidative diabetic wound microenvironment using a nanozyme-reinforced self-protecting hydrogel, ACS Cent. Sci. 5 (3) (2019) 477–485.
[2] X. Zhang, W. Shu, Q. Yu, W. Qu, Y. Wang, R. Li, Functional biomaterials for treatment of chronic wound, Front. Bioeng. Biotechnol. 8 (2020) 516.
[3] Y. Zhang, C. Wen, Y. Liu, A. Li, Q. Guo, X. Zhang, L. Fu, S. Xu, D. Qiao, P. Zheng, NIR responsive composite nanomaterials with in-situ deposition of cascaded nanozymes for multiple synergistic therapy of bacterial infection in diabetic mice, Chem. Eng. J. 470 (2023) 144345.
[4] Y. Zhao, D. Wang, T. Qian, J. Zhang, Z. Li, Q. Gong, X. Ren, Y. Zhao, Biomimetic nanozyme-decorated hydrogels with H2O2-activated oxygenation for modulating immune microenvironment in diabetic wound, ACS Nano 17 (17) (2023) 16854–16869.
[5] A. Joorabloo, T. Liu, Recent advances in reactive oxygen species scavenging nanomaterials for wound healing, Exploration, Wiley Online Library 4 (3) (2024) 20230066.
[6] L. Qiao, Y. Liang, J. Chen, Y. Huang, S.A. Alsareii, A.M. Alamri, F.A. Harraz, B. Guo, Antibacterial conductive self-healing hydrogel wound dressing with dual dynamic bonds promotes infected wound healing, Bioact. Mater. 30 (2023) 129–141.
[7] N. Yang, S. Wang, P. Ding, S. Sun, Q. Wei, H. Jafari, L. Wang, Y. Han, O.V. Okoro, T. Wang, Magnesium-doped biphasic calcium phosphate nanoparticles with incorporation of silver: synthesis, cytotoxic and antibacterial properties, Mater. Lett. 322 (2022) 132478.
[8] M. Tavakolizadeh, A. Pourjavadi, M. Ansari, H. Tebyanian, S.J.S. Tabaei, M. Atarod, N. Rabiee, M. Bagherzadeh, R.S. Varma, An environmentally friendly wound dressing based on a self-healing, extensible and compressible antibacterial hydrogel, Green Chem. 23 (3) (2021) 1312–1329.
[9] X. Kang, Y. Li, Z. Duan, X. Shen, R. Fu, D. Fan, A Mxene@ TA/Fe dual-nanozyme composited antifouling hydrogel for burn wound repair, Chem. Eng. J. 476 (2023) 146420.
[10] X. Wang, T. Liu, M. Chen, Q. Liang, J. Jiang, L. Chen, K. Fan, J. Zhang, L. Gao, An erythrocyte-templated iron single-atom nanozyme for wound healing, Adv. Sci. 11 (6) (2024) 2307844.
[11] Y. Ai, Z.N. Hu, X. Liang, H.b. Sun, H. Xin, Q. Liang, Recent advances in nanozymes: from matters to bioapplications, Adv. Funct. Mater. 32 (14) (2022) 2110432.
[12] D. He, M. Yan, P. Sun, Y. Sun, L. Qu, Z. Li, Recent progress in carbon-dots-based nanozymes for chemosensing and biomedical applications, Chin. Chem. Lett. 32 (10) (2021) 2994–3006, https://doi.org/10.1016/j.cclet.2021.03.078.
[13] H. Sun, Y. Zhou, J. Ren, X. Qu, Carbon nanozymes: enzymatic properties, catalytic mechanism, and applications, Angew. Chem. Int. Ed. Eng. 57 (30) (2018) 9224–9237, https://doi.org/10.1002/anie.201712469.
[14] J. Lou-Franco, B. Das, C. Elliott, C. Cao, Gold Nanozymes: from concept to biomedical applications, Nano Lett. 13 (1) (2020) 10, https://doi.org/10.1007/s40820-020-00532-z.
[15] H. Wang, K. Wan, X. Shi, Recent advances in nanozyme research, Adv. Mater. (Deerfield Beach, Fla.) 31 (45) (2019) e1805368, https://doi.org/10.1002/adma.201805368.
[16] Q. Liu, A. Zhang, R. Wang, Q. Zhang, D. Cui, A review on metal- and metal oxide-based Nanozymes: properties, mechanisms, and applications, Nano Lett. 13 (1) (2021) 154, https://doi.org/10.1007/s40820-021-00674-8.
[17] L. Ma, F. Jiang, X. Fan, L. Wang, C. He, M. Zhou, S. Li, H. Luo, C. Cheng, L. Qiu, Metal-organic-framework-engineered enzyme-mimetic catalysts, Adv. Mater. (Deerfield Beach, Fla.) 32 (49) (2020) e2003065, https://doi.org/10.1002/adma.202003065.
[18] X. Niu, X. Li, Z. Lyu, J. Pan, S. Ding, X. Ruan, W. Zhu, D. Du, Y. Lin, Metal-organic framework based nanozymes: promising materials for biochemical analysis, Chem. Commun. (Camb.) 56 (77) (2020) 11338–11353, https://doi.org/10.1039/d0cc04890a.
[19] J. Chen, X. Liu, G. Zheng, W. Feng, P. Wang, J. Gao, J. Liu, M. Wang, Q. Wang, Detection of glucose based on noble metal nanozymes: mechanism, activity regulation, and enantioselective recognition, Small (Weinheim an der Bergstrasse, Germany) 19 (8) (2023) e2205924, https://doi.org/10.1002/smll.202205924.
[20] J. Chen, Q. Ma, M. Li, D. Chao, L. Huang, W. Wu, Y. Fang, S. Dong, Glucose-oxidase like catalytic mechanism of noble metal nanozymes, Nat. Commun. 12 (1) (2021) 1–9.
[21] L. Zou, X. Li, Y. Huang, C. Wang, Y. Fang, J. Zhao, Q. Jin, J. Ji, Raspberry-like gold nanozyme-hybrid liposomes for hypoxia-enhanced biofilm eradication, Nano Today 50 (2023) 101828.
[22] Z. Xu, J. Chen, Y. Li, T. Hu, L. Fan, J. Xi, J. Han, R. Guo, Yolk-shell Fe3O4@carbon@ platinum-Chlorin e6 nanozyme for MRI-assisted synergistic catalytic-

photodynamic-photothermal tumor therapy, J. Colloid Interface Sci. 628 (2022) 1033–1043.
[23] Y. Zhang, W. Gao, Y. Ma, L. Cheng, L. Zhang, Q. Liu, J. Chen, Y. Zhao, K. Tu, M. Zhang, Integrating Pt nanoparticles with carbon nanodots to achieve robust cascade superoxide dismutase-catalase nanozyme for antioxidant therapy, Nano Today 49 (2023) 101768.
[24] D.-Y. Zhang, H. Liu, M.R. Younis, S. Lei, C. Yang, J. Lin, J. Qu, P. Huang, Ultrasmall platinum nanozymes as broad-spectrum antioxidants for theranostic application in acute kidney injury, Chem. Eng. J. 409 (2021) 127371.
[25] C. Cao, T. Zhang, N. Yang, X. Niu, Z. Zhou, J. Wang, D. Yang, P. Chen, L. Zhong, X. Dong, POD Nanozyme optimized by charge separation engineering for light/pH activated bacteria catalytic/photodynamic therapy, Signal Transduct. Target. Ther. 7 (1) (2022) 86.
[26] B. Zhang, Y. Lv, C. Yu, W. Zhang, S. Song, Y. Li, Y. Chong, J. Huang, Z. Zhang, Au–Pt nanozyme-based multifunctional hydrogel dressing for diabetic wound healing, Biomater. Adv. 137 (2022) 212869.
[27] Z. Wu, C. Huang, Y. Dong, B. Zhao, Y. Chen, Gold core@ platinum shell nanozyme-mediated magnetic relaxation switching DNA sensor for the detection of listeria monocytogenes in chicken samples, Food Control 137 (2022) 108916.
[28] J. Zhang, R. Li, K. Cao, T. Zhang, H. Xiao, L. Wang, Gold and platinum bimetallic nanoparticles with double enzyme-like properties for the colorimetric detection of glutathione, J. Mol. Struct. 1340 (15 September 2025) 142521.
[29] A. Bard, Standard Potentials in Aqueous Solution, Routledge, 2017.
[30] A.R. Deshmukh, H. Aloui, B.S. Kim, Novel biogenic gold nanoparticles catalyzing multienzyme cascade reaction: glucose oxidase and peroxidase mimicking activity, Chem. Eng. J. 421 (2021) 127859.
[31] B. Akkaya, B. Çakiroğlu, M. Özacar, Tannic acid-reduced graphene oxide deposited with Pt nanoparticles for switchable bioelectronics and biosensors based on direct electrochemistry, ACS Sustain. Chem. Eng. 6 (3) (2018) 3805–3814.
[32] C. Chen, H. Yang, X. Yang, Q. Ma, Tannic acid: a crosslinker leading to versatile functional polymeric networks: a review, RSC Adv. 12 (13) (2022) 7689–7711.
[33] S. Ray, R. Biswas, R. Banerjee, P. Biswas, A gold nanoparticle-intercalated mesoporous silica-based nanozyme for the selective colorimetric detection of dopamine, Nanoscale Adv. 2 (2) (2020) 734–745.
[34] A. Mehere, N.B. Chaure, Precisely controlled shape and size of gold nanostructures by seed-mediated reduction reaction method, Appl. Phys. A 126 (2020) 1–14.
[35] H. Jafari, P. Ghaffari-Bohlouli, D. Podstawczyk, L. Nie, A. Shavandi, Tannic acid post-treatment of enzymatically crosslinked chitosan-alginate hydrogels for biomedical applications, Carbohydr. Polym. 295 (2022) 119844.
[36] Z. Qin, Y. Huang, S. Xiao, H. Zhang, Y. Lu, K. Xu, Preparation and characterization of high mechanical strength chitosan/oxidized tannic acid composite film with schiff base and hydrogen bond crosslinking, Int. J. Mol. Sci. 23 (16) (2022) 9284.
[37] J. Liu, S. Dong, S. Gai, Y. Dong, B. Liu, Z. Zhao, Y. Xie, L. Feng, P. Yang, J. Lin, Design and mechanism insight of monodispersed AuCuPt alloy Nanozyme with antitumor activity, ACS Nano 17 (20) (2023) 20402–20423.
[38] J. Chen, Y. Yang, H. Kurban, Y. Xiao, L. Yang, W. Chen, S. He, Platinum coordination complex Nanozymes with ligand-modulated peroxidase-like activity for sensitive biosensing, ACS Appl. Nano Mater. 8 (27) (2025) 13829–13837.
[39] Y. Xue, J. Zhou, Y. Lu, H. Zhang, B. Chen, S. Dong, Y. Xue, K. Zhan, C. Chen, Y. Sun, Advancements in wound management: microenvironment-sensitive bioactive dressings with on-demand regulations for diabetic wounds, Engineering 48 (May 2025) 234–261.
[40] A. Robert, B. Meunier, How to define a nanozyme, ACS Nano 16 (5) (2022) 6956–6959.
[41] J. Guo, Y. Cao, Q.-Y. Wu, Y.-M. Zhou, Y.-H. Cao, L.-S. Cen, Implications of pH and ionic environment in chronic diabetic wounds: an overlooked perspective, Clin. Cosmet. Investig. Dermatol. (2024) 2669–2686.
[42] J. Chen, Q. Ma, M. Li, D. Chao, L. Huang, W. Wu, Y. Fang, S. Dong, Glucose-oxidase like catalytic mechanism of noble metal nanozymes, Nat. Commun. 12 (1) (2021) 3375.
[43] F. Dashtestani, H. Ghourchian, A. Najafi, Silver-gold-apoferritin nanozyme for suppressing oxidative stress during cryopreservation, Mater. Sci. Eng. C 94 (2019) 831–840.
[44] J. Xiang, X. Yang, M. Tan, J. Guo, Y. Ye, J. Deng, Z. Huang, H. Wang, W. Su, J. Cheng, NIR-enhanced Pt single atom/g-C3N4 nanozymes as SOD/CAT mimics to rescue ATP energy crisis by regulating oxidative phosphorylation pathway for delaying osteoarthritis progression, Bioact. Mater. 36 (2024) 1–13.
[45] M.B. de Jesus, Y.L. Kapila, Cellular mechanisms in nanomaterial internalization, intracellular trafficking, and toxicity, Nanotoxicol. Mater. Methodol. Assess. (2013) 201–227. Springer.
[46] Y. Li, Y. Zhang, Z. Zhang, M. Zhang, X. Niu, X. Mao, T. Yue, X. Zhang, Clathrin-mediated endocytosis of multiple nanoparticles tends to be less cooperative: a computational study, J. Phys. Chem. B 128 (40) (2024) 9785–9797.
[47] A. Kumari, J. Sahoo, M. De, 2D-MoS 2-supported copper peroxide nanodots with enhanced nanozyme activity: application in antibacterial activity, Nanoscale 15 (48) (2023) 19801–19814.
[48] Z. Zhou, X. Mei, K. Hu, M. Ma, Y. Zhang, Nanohybrid double network hydrogels based on a platinum nanozyme composite for antimicrobial and diabetic wound healing, ACS Appl. Mater. Interfaces 15 (14) (2023) 17612–17626.
[49] L. Cursi, G. Mirra, L. Boselli, P.P. Pompa, Metrology of platinum nanozymes: mechanistic insights and analytical issues, Adv. Funct. Mater. 34 (24) (2024) 2315587.
[50] Q. Wang, L. Jin, H. Yang, L. Yu, X. Cao, Z. Mao, Bacteria/nanozyme composites: new therapeutics for disease treatment, Small Methods 9 (1) (2024) 2400610.
[51] P. Jiang, L. Zhang, X. Liu, C. Ye, P. Zhu, T. Tan, D. Wang, Y. Wang, Tuning oxidant and antioxidant activities of ceria by anchoring copper single-site for antibacterial application, Nat. Commun. 15 (1) (2024) 1010.
[52] X. Yu, X. Fu, J. Yang, L. Chen, F. Leng, Z. Yang, C. Yu, Glucose/ROS cascade-responsive ceria nanozymes for diabetic wound healing, Mater. Today Bio 15 (2022) 100308.
[53] G. Bardi, L. Boselli, P.P. Pompa, Anti-inflammatory potential of platinum nanozymes: mechanisms and perspectives, Nanoscale 15 (35) (2023) 14284–14300.
[54] Z. Elmazoglu, H. Kayhan, A. Santamaría, E. Rangel-López, P.K. Uğur, A. Ceylan, M. Aschner, Ç. Karasu, Platinum nanoparticles protect against lipopolysaccharide-induced inflammation in microglial BV-2 cells via decreased oxidative damage and increased phagocytosis, Neurochem. Res. 46 (12) (2021) 3325–3341.
[55] F. Gatto, M. Moglianetti, P.P. Pompa, G. Bardi, Platinum nanoparticles decrease reactive oxygen species and modulate gene expression without alteration of immune responses in THP-1 monocytes, Nanomaterials 8 (6) (2018) 392.
[56] B. Jiang, D. Duan, L. Gao, M. Zhou, K. Fan, Y. Tang, J. Xi, Y. Bi, Z. Tong, G.F. Gao, Standardized assays for determining the catalytic activity and kinetics of peroxidase-like nanozymes, Nat. Protoc. 13 (7) (2018) 1506–1520.
[57] P. Ghaffari-Bohlouli, H. Alimoradi, D.F.S. Petri, S. Moghassemi, C.A. Amorim, L. Nie, A. Shavandi, Alleviating hypoxia through self-generating oxygen and hydrogen peroxide fluorinated chitosan: insights from a kinetic study, Chem. Eng. J. 473 (2023) 145072.
[58] L. Shang, Y. Yu, Y. Jiang, X. Liu, N. Sui, D. Yang, Z. Zhu, Ultrasound-augmented multienzyme-like nanozyme hydrogel spray for promoting diabetic wound healing, ACS Nano 17 (16) (2023) 15962–15977.
[59] L. Xu, J. Chen, Q. Ma, D. Chao, X. Zhu, L. Liu, J. Wang, Y. Fang, S. Dong, Critical evaluation of the glucose oxidase-like activity of gold nanoparticles stabilized by different polymers, Nano Res. 16 (4) (2023) 4758–4766.
[60] P. Giannozzi, S. Baroni, N. Bonini, M. Calandra, R. Car, C. Cavazzoni, D. Ceresoli, G.L. Chiarotti, M. Cococcioni, I. Dabo, QUANTUM ESPRESSO: a modular and open-source software project for quantum simulations of materials, J. Phys. Condens. Matter 21 (39) (2009) 395502.
[61] P. Giannozzi, O. Andreussi, T. Brumme, O. Bunau, M.B. Nardelli, M. Calandra, R. Car, C. Cavazzoni, D. Ceresoli, M. Cococcioni, Advanced capabilities for materials modelling with quantum ESPRESSO, J. Phys. Condens. Matter 29 (46) (2017) 465901.
[62] C. Jacobs, S. Onnockx, I. Vandenbroere, I. Pirson, Endogenous SHIP2 does not localize in lipid rafts in 3T3-L1 adipocytes, FEBS Lett. 565 (1) (2004) 70–74, https://doi.org/10.1016/j.febslet.2004.03.076.
[63] H. Jafari, C. Delporte, K.V. Bernaerts, G. De Leener, M. Luhmer, L. Nie, A. Shavandi, Development of marine oligosaccharides for potential wound healing biomaterials engineering, Chem. Eng. J. Adv. 7 (2021) 100113.
[64] R. Bakalova, S. Semkova, D. Ivanova, Z. Zhelev, T. Miller, T. Takeshima, S. Shibata, D. Lazarova, I. Aoki, T. Higashi, Selective targeting of cancerous mitochondria and suppression of tumor growth using redox-active treatment adjuvant, Oxidative Med. Cell. Longev. 2020 (2020).
[65] X. Hao, J. Wu, Y. Shan, M. Cai, X. Shang, J. Jiang, H. Wang, Caveolae-mediated endocytosis of biocompatible gold nanoparticles in living Hela cells, J. Phys. Condens. Matter 24 (16) (2012) 164207.
[66] J. Simińska-Stanny, L. Nicolas, A. Chafai, H. Jafari, M. Hajiabbas, G. Dodi, I. Gardikiotis, C. Delporte, L. Nie, D. Podstawczyk, Advanced PEG-tyramine biomaterial ink for precision engineering of perfusable and flexible small-diameter vascular constructs via coaxial printing, Bioact. Mater. 36 (2024) 168–184.
[67] X. Li, W. Wang, Q. Gao, S. Lai, Y. Liu, S. Zhou, Y. Yan, J. Zhang, H. Wang, J. Wang, Intelligent bacteria-targeting ZIF-8 composite for fluorescence imaging-guided photodynamic therapy of drug-resistant superbug infections and burn wound healing, Exploration (2024) 20230113. Wiley Online Library.